

Difference of Anisotropic and Isotropic TV for Segmentation under Blur and Poisson Noise

Kevin Bui ^{*} Yifei Lou [†] Fredrick Park [‡] Jack Xin [§]

June 21, 2023

Abstract

In this paper, we aim to segment an image degraded by blur and Poisson noise. We adopt a smoothing-and-thresholding (SaT) segmentation framework that finds a piecewise-smooth solution, followed by k -means clustering to segment the image. Specifically for the image smoothing step, we replace the least-squares fidelity for Gaussian noise in the Mumford-Shah model with a maximum posterior (MAP) term to deal with Poisson noise and we incorporate the weighted difference of anisotropic and isotropic total variation (AITV) as a regularization to promote the sparsity of image gradients. For such a nonconvex model, we develop a specific splitting scheme and utilize a proximal operator to apply the alternating direction method of multipliers (ADMM). Convergence analysis is provided to validate the efficacy of the ADMM scheme. Numerical experiments on various segmentation scenarios (grayscale/color and multiphase) showcase that our proposed method outperforms a number of segmentation methods, including the original SaT.

1 Introduction

Image segmentation partitions an image into multiple, coherent regions, where pixels of one region share similar characteristics such as colors, textures, and edges. It remains an important yet challenging problem in computer vision that has various applications, including magnetic resonance imaging [26, 40, 62] and microscopy [7, 81]. One of the most fundamental models for image segmentation is the Mumford-Shah model [50] because of its robustness to noise. Given an input image $f : \Omega \rightarrow \mathbb{R}$ defined on an open, bounded, and connected domain $\Omega \subset \mathbb{R}^2$, the Mumford-Shah model is formulated as

$$\min_{u, \Gamma} E_{MS}(u, \Gamma) := \frac{\lambda}{2} \int_{\Omega} (f - u)^2 dx + \frac{\mu}{2} \int_{\Omega \setminus \Gamma} |\nabla u|^2 dx + \text{Length}(\Gamma), \quad (1)$$

where $u : \Omega \rightarrow \mathbb{R}$ is a piecewise-smooth approximation of the image f , $\Gamma \subset \Omega$ is a compact curve representing the region boundaries, and $\lambda, \mu > 0$ are the weight parameters. The first term in (1) is the fidelity term that ensures that the solution u approximates the image f . The second term enforces u to be piecewise smooth on $\Omega \setminus \Gamma$. The last term measures the perimeter, or more mathematically the one-dimensional Hausdorff

^{*}Department of Mathematics; University of California, Irvine; Irvine, CA 92697, United States; kevinb3@uci.edu

[†]Department of Mathematical Sciences; University of Texas, Dallas; Richardson, TX 75080, United States; yifei.lou@utdallas.edu

[‡]Department of Mathematics & Computer Science; Whittier College; Whittier, CA 90602, United States; fpark@whittier.edu

[§]Department of Mathematics; University of California, Irvine; Irvine, CA 92697, United States; jxin@math.uci.edu

measure in \mathbb{R}^2 [4], of the curve Γ . However, (1) is difficult to solve because the unknown set of boundaries needs to be discretized. One common approach involves approximating the objective function in (1) by a sequence of elliptic functionals [1].

Alternatively, Chan and Vese (CV) [18] simplified (1) by assuming the solution u to be piecewise constant with two phases or regions, thereby making the model easier to solve via the level-set method [51]. Let the level-set function ϕ be Lipschitz continuous and be defined as follows:

$$\begin{cases} \phi(x) > 0 & \text{if } x \text{ is inside } \Gamma, \\ \phi(x) = 0 & \text{if } x \text{ is at } \Gamma, \\ \phi(x) < 0 & \text{if } x \text{ is outside } \Gamma. \end{cases}$$

By the definition of ϕ , the curve Γ is represented by $\phi(x) = 0$. The image region can be defined as either inside or outside the curve Γ . In short, the CV model is formulated as

$$\min_{c_1, c_2, \phi} E_{CV}(c_1, c_2, \phi) := \lambda \left(\int_{\Omega} |f - c_1|^2 H(\phi) dx + \int_{\Omega} |f - c_2|^2 (1 - H(\phi)) dx \right) + \nu \int_{\Omega} |\nabla H(\phi)| dx, \quad (2)$$

where λ, ν are weight parameters, the constants c_1, c_2 are the mean intensity values of the two regions, and $H(\phi)$ is the Heaviside function defined by $H(\phi) = 1$ if $\phi \geq 0$ and $H(\phi) = 0$ otherwise. A convex relaxation [17] of (2) was formulated as

$$\min_{c_1, c_2, u \in [0, 1]} \lambda \left(\int_{\Omega} |f - c_1|^2 u dx + \int_{\Omega} |f - c_2|^2 (1 - u) dx \right) + \nu \int_{\Omega} |\nabla u| dx,$$

where an image segmentation \tilde{u} is obtained by thresholding u , that is

$$\tilde{u}(x) = \begin{cases} 1 & \text{if } u(x) > \tau, \\ 0 & \text{if } u(x) \leq \tau, \end{cases}$$

for some value $\tau \in (0, 1)$. It can be solved efficiently by convex optimization algorithms, such as the alternating direction method of multipliers (ADMM) [6] and primal-dual hybrid gradient [15]. A multiphase extension of (2) was proposed in [64], but it requires that the number of regions to be segmented is a power of 2. For segmenting into an arbitrary number of regions, fuzzy membership functions were incorporated [38].

Cai *et al.* [12] proposed the smoothing-and-thresholding (SaT) framework that is related to the model (1). In the smoothing step of SaT, a convex variant of (1) is formulated as

$$u^* = \arg \min_u \frac{\lambda}{2} \int_{\Omega} (f - Au)^2 dx + \frac{\mu}{2} \int_{\Omega} |\nabla u|^2 dx + \int_{\Omega} |\nabla u| dx, \quad (3)$$

yielding a piecewise-smooth solution u^* . The blurring operator A is included in the case when the image f is blurred. The total variation (TV) term $\int_{\Omega} |\nabla u| dx$ is a convex approximation of the length term in (2) by the coarea formula [17]. After the smoothing step, a thresholding step is applied to the smooth image u^* to segment it into multiple regions. The two-stage framework has many advantages. First, the smoothing model (3) is strongly convex, so it can be solved by any convex optimization algorithm to obtain a unique solution u^* . Second, the user can adjust the number of thresholds to segment u^* and the threshold values to obtain a satisfactory segmentation result, thanks to the flexibility of the thresholding step. Furthermore, the

SaT framework can be adapted to color images by incorporating an intermediate lifting step [10]. Before performing the thresholding step, the lifting step converts the RGB space to Lab (perceived lightness, red-green and yellow-blue) color space and concatenates both RGB and Lab intensity values into a six-channel image. The multi-stage framework for color image segmentation is called smoothing, lifting, and thresholding (SLaT).

One limitation of (3) lies in the ℓ_2 fidelity term that is statistically designed for images corrupted by additive Gaussian noise, and as a result, the smoothing step is not applicable to other types of noise distribution. In this paper, we aim at Poisson noise, which is commonly encountered when an image is taken by photon-capturing devices such as in positron emission tomography [63] and astronomical imaging [36]. By using the data fidelity term of $Au - f \log Au$ [37], we obtain a smoothing model that is appropriate for Poisson noise [16]:

$$\min_u \lambda \int_{\Omega} (Au - f \log Au) dx + \frac{\mu}{2} \int_{\Omega} |\nabla u|^2 dx + \int_{\Omega} |\nabla u| dx. \quad (4)$$

As a convex approximation of the length term in (1), the TV term in (4) can be further improved by nonconvex regularizations. The TV regularization is defined by the ℓ_1 norm of the image gradient. Literature has shown that nonconvex regularizations often yield better performance than the convex ℓ_1 norm in identifying sparse solutions. Examples of nonconvex regularization include $\ell_p, 0 < p < 1$, [13, 20, 77], $\ell_1 - \alpha \ell_2, \alpha \in (0, 1]$ [25, 29, 42, 45, 47], ℓ_1/ℓ_2 [56, 67, 75], and an error function [31]. Lou *et al.* [48] designed a TV version of $\ell_1 - \alpha \ell_2$ called the weighted difference of anisotropic–isotropic total variation (AITV), which outperforms TV in various imaging applications, such as image denoising [48], image reconstruction [48, 42], and image segmentation [8, 9, 74].

In this paper, we propose an AITV variant of (4) to improve the smoothing step of the SaT/SLaT framework for images degraded by Poisson noise and/or blur. Incorporating AITV regularization is motivated by our previous works [8, 9, 53], where we demonstrated that AITV regularization is effective in preserving edges and details, especially under Gaussian and impulsive noise. To maintain similar computational efficiency as the original SaT/SLaT framework, we propose an ADMM algorithm that utilizes the $\ell_1 - \alpha \ell_2$ proximal operator [46]. The main contributions of this paper are as follows:

- We propose an AITV-regularized variant of (4) and prove the existence of a minimizer for the model.
- We develop a computationally efficient ADMM algorithm and provide its convergence analysis under certain conditions.
- We conduct numerical experiments on various grayscale/color images to demonstrate the effectiveness of the proposed approach.

The rest of the paper is organized as follows. Section 2 describes the background information such as notations, Poisson noise, and the SaT/SLaT framework. In Section 3, we propose a simplified Mumford-Shah model with AITV and a MAP data fidelity term for Poisson noise. In the same section, we show that the model has a global minimizer and develop an ADMM algorithm with convergence analysis. In Section 4, we evaluate the performance of the AITV Poisson SaT/SLaT framework on various grayscale and color images. Lastly, we conclude the paper in Section 5.

2 Preliminaries

2.1 Notation

Throughout the rest of the paper, we represent images and mathematical models in discrete notations (i.e., vectors and matrices). An image is represented as an $M \times N$ matrix, and hence the image domain is denoted by $\Omega = \{1, 2, \dots, M\} \times \{1, 2, \dots, N\}$. We define two inner product spaces: $X := \mathbb{R}^{M \times N}$ and $Y := X \times X$. Let $u \in X$. For shorthand notation, we define $u \geq 0$ if $u_{i,j} \geq 0$ for all $(i, j) \in \Omega$. The discrete gradient operator $\nabla : X \rightarrow Y$ is defined by $(\nabla u)_{i,j} = ((\nabla_x u)_{i,j}, (\nabla_y u)_{i,j})$, where

$$(\nabla_x u)_{i,j} = \begin{cases} u_{i,j} - u_{i,j-1} & \text{if } 2 \leq j \leq N, \\ u_{i,1} - u_{i,N} & \text{if } j = 1, \end{cases} \quad \text{and } (\nabla_y u)_{i,j} = \begin{cases} u_{i,j} - u_{i-1,j} & \text{if } 2 \leq i \leq M, \\ u_{1,j} - u_{M,j} & \text{if } i = 1. \end{cases}$$

The space X is equipped with the standard inner product $\langle \cdot, \cdot \rangle_X$ and Euclidean norm $\|\cdot\|_2$. The space Y has the following inner product and norms: for $p = (p_1, p_2) \in Y$ and $q = (q_1, q_2) \in Y$,

$$\begin{aligned} \langle p, q \rangle_Y &= \langle p_1, q_1 \rangle_X + \langle p_2, q_2 \rangle_X, \\ \|p\|_1 &= \sum_{i=1}^M \sum_{j=1}^N |(p_1)_{i,j}| + |(p_2)_{i,j}|, \\ \|p\|_2 &= \sqrt{\sum_{i=1}^M \sum_{j=1}^N |(p_1)_{i,j}|^2 + |(p_2)_{i,j}|^2}, \\ \|p\|_{2,1} &= \sum_{i=1}^M \sum_{j=1}^N \sqrt{(p_1)_{i,j}^2 + (p_2)_{i,j}^2}. \end{aligned}$$

For brevity, we omit the subscript X or Y in the inner product when its context is clear.

2.2 AITV Regularization

There are two popular discretizations of total variation: the isotropic TV [58] and the anisotropic TV [21], which are defined by

$$\begin{aligned} \|\nabla u\|_{2,1} &= \sum_{i=1}^M \sum_{j=1}^N \sqrt{|(\nabla_x u)_{i,j}|^2 + |(\nabla_y u)_{i,j}|^2}, \\ \|\nabla u\|_1 &= \sum_{i=1}^M \sum_{j=1}^N |(\nabla_x u)_{i,j}| + |(\nabla_y u)_{i,j}|, \end{aligned}$$

respectively. This work is based on the weighted difference between anisotropic and isotropic TV (AITV) regularization [48], defined by

$$\|\nabla u\|_1 - \alpha \|\nabla u\|_{2,1} = \sum_{i=1}^M \sum_{j=1}^N \left(|(\nabla_x u)_{i,j}| + |(\nabla_y u)_{i,j}| - \alpha \sqrt{|(\nabla_x u)_{i,j}|^2 + |(\nabla_y u)_{i,j}|^2} \right), \quad (5)$$

for a weighting parameter $\alpha \in [0, 1]$. The range of α ensures the non-negativity of the AITV regularization. Note that anisotropic TV is defined as the ℓ_1 norm of the image gradient $((\nabla_x u)_{i,j}, (\nabla_y u)_{i,j})$ at the pixel

location $(i, j) \in \Omega$, while isotropic TV is the ℓ_2 norm on the gradient vector. As a result, AITV can be viewed as the $\ell_1 - \alpha\ell_2$ regularization on the gradient vector at every pixel, thereby enforcing sparsity individually at each gradient vector.

2.3 Poisson Noise

Poisson noise follows the Poisson distribution with mean and variance η , whose probability mass function is given by

$$\mathbb{P}_\eta(n) = \frac{e^{-\eta}\eta^n}{n!}, \quad n \geq 0. \quad (6)$$

For a clean image $g \in X$, its intensity value at each pixel $g_{i,j}$ serves as the mean and variance for the corresponding noisy observation $f \in X$ defined by

$$f_{i,j} \sim \text{Poisson}(g_{i,j}) \quad \forall (i, j) \in \Omega.$$

To recover the image g from the noisy image f , we find its maximum a posteriori (MAP) estimation u , which maximizes the probability $\mathbb{P}(u|f)$. By Bayes' theorem, we have

$$\mathbb{P}(u|f) = \frac{\mathbb{P}(f|u)\mathbb{P}(u)}{\mathbb{P}(f)}.$$

It further follows from the definition (6) that

$$\mathbb{P}(f_{i,j}|u_{i,j})\mathbb{P}(u_{i,j}) = \mathbb{P}_{u_{i,j}}(f_{i,j})\mathbb{P}(u_{i,j}) = \frac{e^{-u_{i,j}}u_{i,j}^{f_{i,j}}}{(f_{i,j})!}\mathbb{P}(u_{i,j}).$$

Since Poisson noise is i.i.d. pixelwise, we have

$$\mathbb{P}(u|f) = \prod_{(i,j) \in \Omega} \mathbb{P}(f_{i,j}|u_{i,j}) \frac{\mathbb{P}(u_{i,j})}{\mathbb{P}(f_{i,j})} = \prod_{(i,j) \in \Omega} \frac{e^{-u_{i,j}}u_{i,j}^{f_{i,j}}}{(f_{i,j})!} \frac{\mathbb{P}(u_{i,j})}{\mathbb{P}(f_{i,j})}.$$

The MAP estimate of $\mathbb{P}(u|f)$ is equivalent to its negative logarithm, thus leading to the following optimization problem:

$$\min_{u \geq 0} \sum_{(i,j) \in \Omega} u_{i,j} - f_{i,j} \log u_{i,j} - \log \mathbb{P}(u_{i,j}). \quad (7)$$

The last term $-\log \mathbb{P}(u_{i,j})$ can be regarded as an image prior or a regularization. For example, Le *et al.* [37] considered the isotropic total variation as the image prior and proposed a Poisson denoising model

$$\min_{u \geq 0} \langle u - f \log u, \mathbb{1} \rangle + \|\nabla u\|_{2,1}, \quad (8)$$

where \log is applied pixelwise and $\mathbb{1}$ is the matrix whose entries are all 1's. The first term in (8) is a concise notation that is commonly used as a fidelity term for Poisson denoising in various imaging applications [16, 19, 22, 23, 37, 70].

2.4 Review of Poisson SaT/SLaT

A Poisson SaT framework [16] consists of two steps. Given a noisy grayscale image $f \in X$ corrupted by Poisson noise, the first step is the smoothing step that finds a piecewise-smooth solution u^* from the optimization model:

$$u^* = \arg \min_{u \geq 0} \lambda \langle Au - f \log Au, \mathbb{1} \rangle + \frac{\mu}{2} \|\nabla u\|_2^2 + \|\nabla u\|_{2,1}. \quad (9)$$

Then in the thresholding step, $K - 1$ threshold values $\tau_1 \leq \tau_2 \leq \dots \leq \tau_{K-1}$ are appropriately chosen to segment u^* into K regions, where the k th region is given by

$$\Omega_k = \{(i, j) \in \Omega : \tau_{k-1} \leq u_{i,j}^* < \tau_k\},$$

with $\tau_0 := \inf_{x \in \Omega} u^*(x)$. The thresholding step is typically performed by k -means clustering.

The Poisson smoothing, lifting, and thresholding (SLaT) framework [10] extends the Poisson SaT framework to color images. For a color image $f = (f_1, f_2, f_3) \in X \times X \times X$, the model (9) is applied to each color channel f_i for $i = 1, 2, 3$, thus leading to a smoothed color image $u^* = (u_1^*, u_2^*, u_3^*)$. An additional lifting step [49] is performed to transform u^* to (u'_1, u'_2, u'_3) in the Lab space (perceived lightness, red-green, and yellow-blue). The channels in Lab space are less correlated than in RGB space, so they may have useful information for segmentation. The RGB image and the Lab image are concatenated to form the multichannel image $\hat{u} := (u_1^*, u_2^*, u_3^*, u'_1, u'_2, u'_3)$, followed by the thresholding stage. Generally, k -means clustering yields K centroids c_1, \dots, c_K as constant vectors, which are used to form the region

$$\Omega_k = \left\{ (i, j) \in \Omega : \|\hat{u}_{i,j} - c_k\|_2 = \min_{1 \leq \kappa \leq K} \|\hat{u}_{i,j} - c_\kappa\|_2 \right\}$$

for $k = 1, \dots, K$ such that Ω_k 's are disjoint and $\bigcup_{k=1}^K \Omega_k = \Omega$.

After the thresholding step for both SaT/SLaT, we define a piecewise-constant approximation of the image f by

$$\tilde{f} = (\tilde{f}_1, \dots, \tilde{f}_d) \text{ such that } \tilde{f}_\ell = \sum_{k=1}^K c_{k,\ell} \mathbb{1}_{\Omega_k} \quad \forall \ell = 1, \dots, d, \quad (10)$$

where $c_{k,\ell}$ is the ℓ th entry of the constant vector c_k and

$$\mathbb{1}_{\Omega_k} = \begin{cases} 1 & \text{if } (i, j) \in \Omega_k, \\ 0 & \text{if } (i, j) \notin \Omega_k. \end{cases}$$

Recall that $d = 1$ when f is grayscale, and $d = 3$ when f is color.

3 Proposed Approach

To improve the Poisson SaT/SLaT framework, we propose to replace the isotropic TV in (9) with AITV regularization. In other words, in the smoothing step, we obtain the smoothed image u^* from the optimization

Algorithm 1: AITV Poisson SaT/SLaT

1 Input:

- image $f = (f_1, \dots, f_d)$
- blurring operator A
- fidelity parameter $\lambda > 0$
- smoothing parameter $\mu \geq 0$
- AITV parameter $\alpha \in [0, 1]$
- the number of regions in the image K

2 Output: Segmentation \tilde{f} **3** Stage one: Compute u_ℓ by solving (11) separately for $\ell = 1, \dots, d$.**4** Stage two: **if** f is a grayscale image, i.e., $d = 1$ **then****5** | Go to stage three.**6** **else if** f is a color image, i.e., $d = 3$ **then****7** | Transfer the solution $u^* = (u_1^*, u_2^*, u_3^*)$ into Lab space to obtain (u'_1, u'_2, u'_3) and concatenate to form $\hat{u} = (u_1^*, u_2^*, u_3^*, u'_1, u'_2, u'_3)$.**8** Stage three: Apply k -means to obtain $\{(c_k, \Omega_k)\}_{k=1}^K$ and compute \tilde{f} by (10).

problem

$$u^* = \arg \min_u F(u) := \lambda \langle Au - f \log Au, \mathbb{1} \rangle + \frac{\mu}{2} \|\nabla u\|_2^2 + \|\nabla u\|_1 - \alpha \|\nabla u\|_{2,1}, \quad (11)$$

for $\alpha \in [0, 1]$. We establish that this model admits a global solution. We then develop an ADMM algorithm to find a solution and provide the convergence analysis. The overall segmentation approach is described in Algorithm 1.

3.1 Model Analysis

To establish the solution's existence of the proposed model (11), we start with Lemma 1, a discrete version of Poincaré's inequality [27]. In addition, we prove Lemma 2 and Proposition 3, leading to the global existence theorem (Theorem 4).

Lemma 1. *There exists a constant $C > 0$ such that*

$$\|u - \bar{u}\mathbb{1}\|_2 \leq C \|\nabla u\|_{2,1}, \quad (12)$$

for every $u \in X$ and $\bar{u} := \frac{1}{MN} \sum_{i=1}^M \sum_{j=1}^N u_{i,j}$.

Proof. We prove it by contradiction. Suppose there exists a sequence $\{u_k\}_{k=1}^\infty$ such that

$$\|u_k - \bar{u}_k \mathbb{1}\|_2 > k \|\nabla u_k\|_{2,1}, \quad (13)$$

where $\bar{u}_k = \frac{1}{MN} \sum_{i=1}^M \sum_{j=1}^N (u_k)_{i,j}$. For every k , we normalize each element in the sequence by $v_k = \frac{u_k - \bar{u}_k \mathbb{1}}{\|u_k - \bar{u}_k \mathbb{1}\|_2}$.

It is straightforward that

$$\bar{v}_k = \frac{1}{MN} \sum_{i=1}^M \sum_{j=1}^N (v_k)_{i,j} = 0, \quad \|v_k\|_2 = 1 \quad \forall k \in \mathbb{N}. \quad (14)$$

By (13), we have

$$\|\nabla v_k\|_{2,1} < \frac{1}{k}. \quad (15)$$

As $\{v_k\}_{k=1}^\infty$ is bounded, there exists a convergent subsequence $\{v_{k_j}\}_{j=1}^\infty$ such that $v_{k_j} \rightarrow v^*$ for $v^* \in X$. It follows from (15) that $\|\nabla v^*\|_{2,1} = 0$. Since $\ker(\nabla) = \{c\mathbb{1} : c \in \mathbb{R}\}$, then v^* is a constant vector. However, (14) implies that $\bar{v}^* = 0$ and $\|v^*\|_2 = 1$. This contradiction proves the lemma. \square

Lemma 2. *Suppose $\|f\|_\infty < \infty$ and $\min_{i,j} f_{i,j} > 0$. There exists a scalar $u_0 > 0$ such that we have $2(x - f_{i,j} \log x) \geq x$ for any $x \geq u_0$ and $(i, j) \in \Omega$.*

Proof. For each $(i, j) \in \Omega$, we want to show that there exists $u_{i,j} > 0$ such that $H(x) := x - 2f_{i,j} \log x \geq 0$ for $x \geq u_{i,j}$. Since $H(x)$ is strictly convex and it attains a global minimum at $x = 2f_{i,j}$, it is increasing on the domain $x > 2f_{i,j}$. Additionally as x dominates $\log(x)$ as $x \rightarrow +\infty$, there exists $u_{i,j} > 2f_{i,j} > 0$ such that $\frac{u_{i,j}}{\log u_{i,j}} \geq 2f_{i,j}$, which implies that $H(u_{i,j}) = u_{i,j} - 2f_{i,j} \log u_{i,j} \geq 0$. As a result, for $x \geq u_{i,j} > 2f_{i,j}$, we obtain $x - 2f_{i,j} \log x = H(x) \geq H(u_{i,j}) \geq 0$. Define $u_0 := \max_{i,j} u_{i,j}$, and hence we have $2(x - f_{i,j} \log x) \geq x$ for $x \geq u_0 \geq u_{i,j}, \forall (i, j) \in \Omega$. \square

Proposition 3. *Suppose $\ker(A) \cap \ker(\nabla) = \{0\}$ and $\{u_k\}_{k=1}^\infty \subset X$. If $\{(Au_k, \nabla u_k)\}_{k=1}^\infty$ is bounded, then $\{\bar{u}_k\}_{k=1}^\infty$ is bounded.*

Proof. Since $\ker(A) \cap \ker(\nabla) = \{0\}$, we have $A\mathbb{1} \neq 0$. Simple calculations lead to

$$\begin{aligned} \|\bar{u}_k\| \|A\mathbb{1}\|_2 &= \|A(\bar{u}_k \mathbb{1})\|_2 \leq \|A(\bar{u}_k \mathbb{1} - u_k)\|_2 + \|Au_k\|_2 \\ &\leq \|A\| \|u_k - \bar{u}_k \mathbb{1}\|_2 + \|Au_k\|_2 \\ &\leq C \|A\| \|\nabla u_k\|_{2,1} + \|Au_k\|_2, \end{aligned} \quad (16)$$

where the last inequality is due to Lemma 1. The boundedness of $\{Au_k\}_{k=1}^\infty$ and $\{\nabla u_k\}_{k=1}^\infty$ implies that $\{\bar{u}_k\}_{k=1}^\infty$ is also bounded by (16). We apply Lemma 1 to obtain

$$\|u_k\|_2 \leq \|u_k - \bar{u}_k \mathbb{1}\|_2 + \|\bar{u}_k \mathbb{1}\|_2 < C \|\nabla u_k\|_{2,1} + \|\bar{u}_k \mathbb{1}\|_2 < \infty,$$

which thereby proves that $\{u_k\}_{k=1}^\infty$ is bounded. \square

Finally, we adapt the proof in [16] to establish that F has a global minimizer.

Theorem 4. *Suppose $\|f\|_\infty < \infty$ and $\min_{i,j} f_{i,j} > 0$. If $\lambda > 0, \mu \geq 0, \alpha \in [0, 1)$, and $\ker(A) \cap \ker(\nabla) = \{0\}$, then F has a global minimizer.*

Proof. It is straightforward that $\|\nabla u\|_{2,1} \leq \|\nabla u\|_1$, thus $\|\nabla u\|_1 - \alpha \|\nabla u\|_{2,1} \geq 0$ for $\alpha \in [0, 1)$. As a result, we have

$$F(u) \geq \lambda \langle Au - f \log Au, \mathbb{1} \rangle = \lambda \sum_{i=1}^M \sum_{j=1}^N (Au)_{i,j} - f_{i,j} \log (Au)_{i,j}.$$

Given a scalar $f > 0$, the function $G(x) = x - f \log(x)$ attains its global minimum at $x = f$. Therefore, we have $x - f_{i,j} \log x \geq f_{i,j} - f_{i,j} \log f_{i,j}$ for all $x > 0$ and $(i, j) \in \Omega$, which leads to a lower bound of $F(u)$, i.e.,

$$F(u) \geq \lambda \sum_{i=1}^M \sum_{j=1}^N (Au)_{i,j} - f_{i,j} \log (Au)_{i,j} \geq \lambda \sum_{i=1}^M \sum_{j=1}^N f_{i,j} - f_{i,j} \log f_{i,j} =: F_0. \quad (17)$$

As $F(u)$ is lower bounded by F_0 , we can choose a minimizing sequence $\{u_k\}_{k=1}^\infty$ and hence $F(u_k)$ has a uniform upper bound, denoted by B_1 , i.e., $F(u_k) < B_1$ for all $k \in \mathbb{N}$. It further follows from (17) that

$$B_1 \geq F(u_k) \geq \lambda \langle Au_k - f \log Au_k, \mathbb{1} \rangle \geq F_0,$$

which implies that $\{\lambda \langle Au_k - f \log Au_k, \mathbb{1} \rangle\}_{k=1}^\infty$ is uniformly bounded, i.e., there exists a constant $B_2 > 0$ such that $|\langle Au_k - f \log Au_k, \mathbb{1} \rangle| < B_2, \forall k$. Using these uniform bounds, we derive that

$$(1 - \alpha) \|\nabla u_k\|_1 \leq \frac{\mu}{2} \|\nabla u_k\|_2^2 + \|\nabla u_k\|_1 - \alpha \|\nabla u_k\|_{2,1} = F(u_k) - \lambda \langle Au_k - f \log Au_k, \mathbb{1} \rangle \leq B_1 + \lambda B_2.$$

As $\alpha < 1$, the sequence $\{\nabla u_k\}_{k=1}^\infty$ is bounded.

To prove the boundedness of $\{Au_k\}_{k=1}^\infty$, we introduce the notations of $x^+ = \max(x, 0)$ and $x^- = -\min(x, 0)$ for any $x \in \mathbb{R}$. Then $x = x^+ - x^-$. By Lemma 2, there exists $u_0 > 0$ such that $2(x - f_{i,j} \log x) \geq x, \forall x \geq u_0$ and $(i, j) \in \Omega$. We observe that

$$\begin{aligned} \|Au_k\|_1 &= \sum_{i=1}^M \sum_{j=1}^N |(Au_k)_{i,j}| \leq \sum_{i=1}^M \sum_{j=1}^N \max\{2((Au_k)_{i,j} - f_{i,j} \log (Au_k)_{i,j}), u_0\} \\ &\leq 2 \sum_{i=1}^M \sum_{j=1}^N ((Au_k)_{i,j} - f_{i,j} \log (Au_k)_{i,j})^+ + MNu_0 \\ &= 2 \sum_{i=1}^M \sum_{j=1}^N \left[((Au_k)_{i,j} - f_{i,j} \log (Au_k)_{i,j}) + ((Au_k)_{i,j} - f_{i,j} \log (Au_k)_{i,j})^- \right] + MNu_0 \quad (18) \\ &= 2 \langle Au_k - f \log Au_k, \mathbb{1} \rangle + 2 \sum_{i=1}^M \sum_{j=1}^N ((Au_k)_{i,j} - f_{i,j} \log (Au_k)_{i,j})^- + MNu_0 \\ &\leq 2B_2 + 2 \sum_{i=1}^M \sum_{j=1}^N |f_{i,j} - f_{i,j} \log f_{i,j}| + MNu_0 < \infty. \end{aligned}$$

This shows that $\{Au_k\}_{k=1}^\infty$ is bounded.

Since both $\{\nabla u_k\}_{k=1}^\infty$ and $\{Au_k\}_{k=1}^\infty$ are bounded, then $\{u_k\}_{k=1}^\infty$ is bounded due to Proposition 3. Therefore, there exists a subsequence $\{u_{k_n}\}_{n=1}^\infty$ that converges to some $u^* \in X$. As F is continuous and thus lower semicontinuous, we have

$$F(u^*) \leq \liminf_{n \rightarrow \infty} F(u_{k_n}),$$

which means that u^* minimizes F . □

3.2 Numerical Algorithm

To minimize (11), we introduce two auxiliary variables $v \in X$ and $w = (w_x, w_y) \in Y$, leading to an equivalent constrained optimization problem:

$$\begin{aligned} \min_{u,v,w} \quad & \lambda \langle v - f \log v, \mathbb{1} \rangle + \frac{\mu}{2} \|\nabla u\|_2^2 + \|w\|_1 - \alpha \|w\|_{2,1} \\ \text{s.t.} \quad & Au = v, \quad \nabla u = w. \end{aligned} \quad (19)$$

The corresponding augmented Lagrangian is expressed as

$$\begin{aligned} \mathcal{L}_{\beta_1, \beta_2}(u, v, w, y, z) = & \lambda \langle v - f \log v, \mathbb{1} \rangle + \frac{\mu}{2} \|\nabla u\|_2^2 + \|w\|_1 - \alpha \|w\|_{2,1} \\ & + \langle y, Au - v \rangle + \frac{\beta_1}{2} \|Au - v\|_2^2 + \langle z, \nabla u - w \rangle + \frac{\beta_2}{2} \|\nabla u - w\|_2^2, \end{aligned} \quad (20)$$

where $y \in X$ and $z = (z_x, z_y) \in Y$ are Lagrange multipliers and β_1, β_2 are positive parameters. We then apply the alternating direction method of multipliers (ADMM) to minimize (19) that consists of the following steps per iteration k :

$$u_{k+1} = \arg \min_u \mathcal{L}_{\beta_1, k, \beta_2, k}(u, v_k, w_k, y_k, z_k), \quad (21a)$$

$$v_{k+1} = \arg \min_v \mathcal{L}_{\beta_1, k, \beta_2, k}(u_{k+1}, v, w_k, y_k, z_k), \quad (21b)$$

$$w_{k+1} = \arg \min_w \mathcal{L}_{\beta_1, k, \beta_2, k}(u_{k+1}, v_{k+1}, w, y_k, z_k), \quad (21c)$$

$$y_{k+1} = y_k + \beta_{1,k}(Au_{k+1} - v_{k+1}), \quad (21d)$$

$$z_{k+1} = z_k + \beta_{2,k}(\nabla u_{k+1} - w_{k+1}), \quad (21e)$$

$$(\beta_{1,k+1}, \beta_{2,k+1}) = \sigma(\beta_{1,k}, \beta_{2,k}), \quad (21f)$$

where $\sigma > 1$.

Remark 1. *The scheme presented in (21) slightly differs from the original ADMM [6], the latter of which has $\sigma = 1$ in (21f). Having $\sigma > 1$ increases the weights of the penalty parameters $\beta_{1,k}, \beta_{2,k}$ in each iteration k , thus accelerating the numerical convergence speed of the proposed ADMM algorithm. A similar technique has been used in [14, 30, 60, 61, 79].*

All the subproblems (21a)-(21c) have closed-form solutions. In particular, the first-order optimality condition for (21a) is

$$[\beta_{1,k} A^\top A - (\mu + \beta_{2,k}) \Delta] u^{k+1} = A^\top (\beta_{1,k} v_k - y_k) - \nabla^\top (z_k - \beta_{2,k} w_k), \quad (22)$$

where $\Delta = -\nabla^\top \nabla$ is the Laplacian operator. If $\ker(A) \cap \ker(\nabla) = \{0\}$, then $\beta_{1,k} A^\top A - (\mu + \beta_{2,k}) \Delta$ is positive definite and thereby invertible, which implies that (22) has a unique solution u^{k+1} . By assuming periodic boundary condition for u , the operators Δ and $A^\top A$ are block circulant [68], and hence (22) can be solved efficiently by the 2D discrete Fourier transform \mathcal{F} . Specifically, we have the formula

$$u_{k+1} = \mathcal{F}^{-1} \left(\frac{\mathcal{F}(A)^* \circ \mathcal{F}(\beta_{1,k} v_k - y_k) - \mathcal{F}(\nabla)^* \circ \mathcal{F}(z_k - \beta_{2,k} w_k)}{\beta_{1,k} \mathcal{F}(A)^* \circ \mathcal{F}(A) - (\mu + \beta_{2,k}) \mathcal{F}(\Delta)} \right), \quad (23)$$

where \mathcal{F}^{-1} is the inverse discrete Fourier transform, the superscript $*$ denotes complex conjugate, the

operation \circ is componentwise multiplication, and division is componentwise. By differentiating the objective function of (21b) and setting it to zero, we can get a closed-form solution for v_{k+1} given by

$$v_{k+1} = \frac{(\beta_{1,k} A u_{k+1} + y_k - \lambda \mathbb{1}) + \sqrt{(\beta_{1,k} A u_{k+1} + y_k - \lambda \mathbb{1})^2 + 4\lambda\beta_{1,k}f}}{2\beta_{1,k}}, \quad (24)$$

where the square root, squaring, and division are performed componentwise. Lastly, the w -subproblem (21c) can be decomposed componentwise as follows:

$$\begin{aligned} (w_{i,j})_{k+1} &= \arg \min_{w_{i,j}} \|w_{i,j}\|_1 - \alpha \|w_{i,j}\|_2 + \frac{\beta_{2,k}}{2} \left\| w_{i,j} - \left((\nabla u_{k+1})_{i,j} + \frac{(z_k)_{i,j}}{\beta_{2,k}} \right) \right\|_2^2 \\ &= \text{prox} \left((\nabla u_{k+1})_{i,j} + \frac{(z_k)_{i,j}}{\beta_{2,k}}, \alpha, \frac{1}{\beta_{2,k}} \right), \end{aligned} \quad (25)$$

where the proximal operator for $\ell_1 - \alpha\ell_2$ on $x \in \mathbb{R}^n$ is given by

$$\text{prox}(x, \alpha, \beta) = \arg \min_y \|y\|_1 - \alpha \|y\|_2 + \frac{1}{2\beta} \|x - y\|_2^2. \quad (26)$$

The proximal operator for $\ell_1 - \alpha\ell_2$ has a closed form solution summarized by Lemma 5.

Lemma 5 ([46]). *Given $x \in \mathbb{R}^n$, $\beta > 0$, and $\alpha \in [0, 1]$, the optimal solution to (26) is given by one of the following cases:*

1. When $\|x\|_\infty > \beta$, we have

$$x^* = (\|\xi\|_2 + \alpha\beta) \frac{\xi}{\|\xi\|_2},$$

where $\xi = \text{sign}(x) \circ \max(|x| - \beta, 0)$.

2. When $(1 - \alpha)\beta < \|x\|_\infty \leq \beta$, then x^* is a 1-sparse vector such that one chooses $i \in \arg \max_j (|x_j|)$ and defines $x_i^* = (|x_i| + (\alpha - 1)\beta) \text{sign}(x_i)$ and the remaining elements equal to 0.

3. When $\|x\|_\infty \leq (1 - \alpha)\beta$, then $x^* = 0$.

In summary, we describe the ADMM scheme to solve (11) in Algorithm 2.

3.3 Convergence Analysis

We establish the subsequential convergence of ADMM described in Algorithm 2. The global convergence of ADMM [69] is inapplicable to our model as the gradient operator ∇ is non-surjective, which will be further investigated in future work. For the sake of brevity, we set $\beta = \beta_1 = \beta_2$ and denote

$$\mathcal{L}_\beta(u, v, w, y, z) := \mathcal{L}_{\beta,\beta}(u, v, w, y, z).$$

In addition, we introduce definitions of subdifferentials [57], which defines a stationary point of a non-smooth objective function.

Definition 6. *For a proper function $h : \mathbb{R}^n \rightarrow \mathbb{R} \cup \{+\infty\}$, define $\text{dom}(h) := \{x \in \mathbb{R}^n : h(x) < +\infty\}$.*

Algorithm 2: ADMM for the AITV-Regularized Smoothing Model with Poisson Fidelity (11)

1 Input:

- image f
- blurring operator A
- fidelity parameter $\lambda > 0$
- smoothing parameter $\mu \geq 0$
- AITV parameter $\alpha \in [0, 1]$
- penalty parameters $\beta_{1,0}, \beta_{2,0} > 0$
- penalty multiplier $\sigma > 1$
- relative error $\epsilon > 0$

2 Output: u_k
3 Initialize u_0, w_0, z_0 .

4 Set $k = 0$.

5 **while** $\frac{\|u_k - u_{k-1}\|_2}{\|u_k\|_2} > \epsilon$ **do**
6

$$\begin{aligned}
 u_{k+1} &= \mathcal{F}^{-1} \left(\frac{\mathcal{F}(A)^* \circ \mathcal{F}(\beta_{1,k} v_k - y_k) - \mathcal{F}(\nabla)^* \circ \mathcal{F}(z_k - \beta_{2,k} w_k)}{\beta_{1,k} \mathcal{F}(A)^* \circ \mathcal{F}(A) - (\mu + \beta_{2,k}) \mathcal{F}(\Delta)} \right) \\
 v_{k+1} &= \frac{(\beta_{1,k} A u_{k+1} + y_k - \lambda \mathbb{1}) + \sqrt{(\beta_{1,k} A u_{k+1} + y_k - \lambda \mathbb{1})^2 + 4\lambda \beta_{1,k} f}}{2\beta_{1,k}} \\
 (w_{k+1})_{i,j} &= \text{prox} \left((\nabla u_{k+1})_{i,j} + \frac{(z_k)_{i,j}}{\beta_{2,k}}, \alpha, \frac{1}{\beta_{2,k}} \right) \quad \forall (i, j) \in \Omega \\
 y_{k+1} &= y_k + \beta_{1,k} (A u_{k+1} - v_{k+1}) \\
 z_{k+1} &= z_k + \beta_{2,k} (\nabla u_{k+1} - w_{k+1}) \\
 (\beta_{1,k+1}, \beta_{2,k+1}) &= \sigma(\beta_{1,k}, \beta_{2,k}) \\
 k &:= k + 1
 \end{aligned}$$

(a) The regular subdifferential at $x \in \text{dom}(h)$ is given by

$$\hat{\partial}h(x) := \left\{ w : \liminf_{x' \rightarrow x, x' \neq x} \frac{h(x') - h(x) - \langle w, x' - x \rangle}{\|x' - x\|} \geq 0 \right\}.$$

(b) The (limiting) subdifferential at $x \in \text{dom}(h)$ is given by

$$\partial h(x) := \left\{ w : \exists x_k \rightarrow x \text{ and } w_k \in \hat{\partial}h(x_k) \text{ with } w_k \rightarrow w \text{ and } h(x_k) \rightarrow h(x) \right\}.$$

An important property of the limiting subdifferential is its closedness: for any $(x_k, v_k) \rightarrow (x, v)$ with $v_k \in \partial h(x_k)$, if $h(x_k) \rightarrow h(x)$, then $v \in \partial h(x)$.

Lemma 7. Suppose that $\ker(A) \cap \ker(\nabla) = \{0\}$ and $0 \leq \alpha < 1$. Let $\{(u_k, v_k, w_k, y_k, z_k)\}_{k=1}^{\infty}$ be a sequence

generated by Algorithm 2. Then we have

$$\begin{aligned} & \mathcal{L}_{\beta_{k+1}}(u_{k+1}, v_{k+1}, w_{k+1}, y_{k+1}, z_{k+1}) - \mathcal{L}_{\beta_k}(u_k, v_k, w_k, y_k, z_k) \\ & \leq -\frac{\nu}{2} \|u_{k+1} - u_k\|_2^2 - \frac{\beta_0}{2} \|v_{k+1} - v_k\|_2^2 + \frac{1}{\sigma^{k-1}\beta_0} \left(\|y_{k+1} - y_k\|_2^2 + \|z_{k+1} - z_k\|_2^2 \right), \end{aligned} \quad (28)$$

for some constant $\nu > 0$.

Proof. If $\ker(A) \cap \ker(\nabla) = \{0\}$, then $\beta_0 A^\top A + (\beta_0 + \mu)\nabla^\top \nabla$ is positive definite, and hence there exists $\nu > 0$ such that

$$\beta_k \|Au\|_2^2 + (\beta_k + \mu)\|\nabla u\|_2^2 \geq \beta_0 \|Au\|_2^2 + (\beta_0 + \mu)\|\nabla u\|_2^2 \geq \nu \|u\|_2^2 \quad \forall k \in \mathbb{N},$$

which implies that $\mathcal{L}_{\beta_k}(u, v, w_k, y_k, z_k)$ is strongly convex with respect to u with parameter ν . Additionally, $\mathcal{L}_{\beta_k}(u_{k+1}, v, w_k, y_k, z_k)$ is strongly convex with respect to v with parameter $\beta_0 \leq \beta_k$. It follows from [5, Theorem 5.25] that we have

$$\mathcal{L}_{\beta_k}(u_{k+1}, v_k, w_k, y_k, z_k) - \mathcal{L}_{\beta_k}(u_k, v_k, w_k, y_k, z_k) \leq -\frac{\nu}{2} \|u_{k+1} - u_k\|_2^2, \quad (29)$$

$$\mathcal{L}_{\beta_k}(u_{k+1}, v_{k+1}, w_k, y_k, z_k) - \mathcal{L}_{\beta_k}(u_{k+1}, v_k, w_k, y_k, z_k) \leq -\frac{\beta_0}{2} \|v_{k+1} - v_k\|_2^2. \quad (30)$$

As w_{k+1} is the optimal solution to (21c), it is straightforward to have

$$\mathcal{L}_{\beta_k}(u_{k+1}, v_{k+1}, w_{k+1}, y_k, z_k) - \mathcal{L}_{\beta_k}(u_{k+1}, v_{k+1}, w_k, y_k, z_k) \leq 0. \quad (31)$$

Simple calculations by using (21d)-(21e) lead to

$$\begin{aligned} & \mathcal{L}_{\beta_k}(u_{k+1}, v_{k+1}, w_{k+1}, y_{k+1}, z_{k+1}) - \mathcal{L}_{\beta_k}(u_{k+1}, v_{k+1}, w_{k+1}, y_k, z_k) \\ & = (\mathcal{L}_{\beta_k}(u_{k+1}, v_{k+1}, w_{k+1}, y_{k+1}, z_{k+1}) - \mathcal{L}_{\beta_k}(u_{k+1}, v_{k+1}, w_{k+1}, y_{k+1}, z_k)) \\ & \quad + (\mathcal{L}_{\beta_k}(u_{k+1}, v_{k+1}, w_{k+1}, y_{k+1}, z_k) - \mathcal{L}_{\beta_k}(u_{k+1}, v_{k+1}, w_{k+1}, y_k, z_k)) \\ & = \langle z_{k+1} - z_k, \nabla u_{k+1} - w_{k+1} \rangle + \langle y_{k+1} - y_k, Au_{k+1} - v_{k+1} \rangle \\ & = \frac{1}{\beta_k} \left(\|y_{k+1} - y_k\|_2^2 + \|z_{k+1} - z_k\|_2^2 \right). \end{aligned} \quad (32)$$

Lastly, we have

$$\begin{aligned} & \mathcal{L}_{\beta_{k+1}}(u_{k+1}, v_{k+1}, w_{k+1}, y_{k+1}, z_{k+1}) - \mathcal{L}_{\beta_k}(u_{k+1}, v_{k+1}, w_{k+1}, y_{k+1}, z_{k+1}) \\ & = \frac{\beta_{k+1} - \beta_k}{2} \left(\|Au_{k+1} - v_{k+1}\|_2^2 + \|\nabla u_{k+1} - w_{k+1}\|_2^2 \right) \\ & = \frac{\beta_{k+1} - \beta_k}{2\beta_k^2} \left(\|y_{k+1} - y_k\|_2^2 + \|z_{k+1} - z_k\|_2^2 \right). \end{aligned} \quad (33)$$

Combining (29) - (33) together with the fact that $\beta_k = \sigma^k \beta_0$ for $\sigma > 1$, we obtain

$$\begin{aligned} & \mathcal{L}_{\beta_{k+1}}(u_{k+1}, v_{k+1}, w_{k+1}, y_{k+1}, z_{k+1}) - \mathcal{L}_{\beta_k}(u_k, v_k, w_k, y_k, z_k) \\ & \leq -\frac{\nu}{2} \|u_{k+1} - u_k\|_2^2 - \frac{\beta_0}{2} \|v_{k+1} - v_k\|_2^2 + \frac{\beta_{k+1} + \beta_k}{2\beta_k^2} \left(\|y_{k+1} - y_k\|_2^2 + \|z_{k+1} - z_k\|_2^2 \right) \end{aligned}$$

$$\begin{aligned}
&= -\frac{\nu}{2}\|u_{k+1} - u_k\|_2^2 - \frac{\beta_0}{2}\|v_{k+1} - v_k\|_2^2 + \frac{\sigma + 1}{2\sigma^k\beta_0} \left(\|y_{k+1} - y_k\|_2^2 + \|z_{k+1} - z_k\|_2^2 \right) \\
&\leq -\frac{\nu}{2}\|u_{k+1} - u_k\|_2^2 - \frac{\beta_0}{2}\|v_{k+1} - v_k\|_2^2 + \frac{1}{\sigma^{k-1}\beta_0} \left(\|y_{k+1} - y_k\|_2^2 + \|z_{k+1} - z_k\|_2^2 \right).
\end{aligned}$$

This completes the proof. \square

Lemma 8. *Suppose that $\ker(A) \cap \ker(\nabla) = \{0\}$ and $0 \leq \alpha < 1$. Let $\{(u_k, v_k, w_k, y_k, z_k)\}_{k=1}^\infty$ be generated by Algorithm 2. If $\{y_k\}_{k=1}^\infty$ bounded, then the sequence $\{(u_k, v_k, w_k, y_k, z_k)\}_{k=1}^\infty$ is bounded, $u_{k+1} - u_k \rightarrow 0$, and $v_{k+1} - v_k \rightarrow 0$.*

Proof. First we show that $\{z_k\}_{k=1}^\infty$ is bounded. Combining (21e) with the first-order optimality condition of (25), we have

$$\begin{aligned}
(z_{k+1})_{i,j} &= (z_k)_{i,j} + \beta_k ((\nabla u_{k+1})_{i,j} - (w_{k+1})_{i,j}) \in \partial(\|(w_{k+1})_{i,j}\|_1 - \alpha\|(w_{k+1})_{i,j}\|_2) \\
&\subseteq \partial(\|(w_{k+1})_{i,j}\|_1) - \alpha\partial(\|(w_{k+1})_{i,j}\|_2),
\end{aligned} \tag{34}$$

which implies that there exist $\xi_1 \in \partial\|(w_{k+1})_{i,j}\|_1$ and $\xi_2 \in \partial\|(w_{k+1})_{i,j}\|_2$ such that $(z_{k+1})_{i,j} = \xi_1 - \alpha\xi_2$ for each $(i, j) \in \Omega$. Recall that for $x \in \mathbb{R}^2$ the subgradients of the two norms are

$$\partial\|x\|_1 = \left\{ \xi \in \mathbb{R}^2 : \xi_i = \begin{cases} \text{sign}(x_i) & \text{if } x_i \neq 0 \\ \xi_i \in [-1, 1] & \text{if } x_i = 0 \end{cases} \text{ for } i = 1, 2 \right\}, \tag{35}$$

$$\partial\|x\|_2 = \left\{ \xi \in \mathbb{R}^2 : \xi = \begin{cases} \frac{x}{\|x\|_2} & \text{if } x \neq 0 \\ \in \{\xi \in \mathbb{R}^2 : \|\xi\|_2 \leq 1\} & \text{if } x = 0 \end{cases} \right\}. \tag{36}$$

Therefore, we have $\|\xi_1\|_\infty \leq 1$, $\|\xi_2\|_\infty \leq 1$, and hence $\|(z_{k+1})_{i,j}\|_\infty \leq 1 + \alpha$ (by the triangle inequality), i.e., $\{z_k\}_{k=1}^\infty$ is bounded.

By the assumption $\{y_k\}_{k=1}^\infty$ is bounded. There exist two constants $C_1, C_2 > 0$ such that $\|y_{k+1} - y_k\|_2^2 \leq C_1$, $\|z_{k+1} - z_k\|_2^2 \leq C_1$, $\|y_k\|_2^2 \leq C_2$, and $\|z_k\|_2^2 \leq C_2$ for all $k \in \mathbb{N}$. Hence, we have from (28) that

$$\begin{aligned}
\mathcal{L}_{\beta_{k+1}}(u_{k+1}, v_{k+1}, w_{k+1}, y_{k+1}, z_{k+1}) &\leq \mathcal{L}_{\beta_k}(u_k, v_k, w_k, y_k, z_k) - \frac{\nu}{2}\|u_{k+1} - u_k\|_2^2 \\
&\quad - \frac{\beta_0}{2}\|v_{k+1} - v_k\|_2^2 + \frac{2C_1}{\sigma^{k-1}\beta_0}.
\end{aligned} \tag{37}$$

A telescoping summation of (37) leads to

$$\begin{aligned}
\mathcal{L}_{\beta_{k+1}}(u_{k+1}, v_{k+1}, w_{k+1}, y_{k+1}, z_{k+1}) &\leq \mathcal{L}_{\beta_0}(u_0, v_0, w_0, y_0, z_0) + \frac{2C_1}{\beta_0} \sum_{i=0}^k \frac{1}{\sigma^{i-1}} \\
&\quad - \frac{\nu}{2} \sum_{i=0}^k \|u_{i+1} - u_i\|_2^2 - \frac{\beta_0}{2} \sum_{i=0}^k \|v_{i+1} - v_i\|_2^2.
\end{aligned} \tag{38}$$

By completing two least-squares terms, we can rewrite $\mathcal{L}_{\beta_{k+1}}$ as

$$\begin{aligned} \mathcal{L}_{\beta_{k+1}}(u_{k+1}, v_{k+1}, w_{k+1}, y_{k+1}, z_{k+1}) &= \lambda \langle v_{k+1} - f \log v_{k+1}, \mathbb{1} \rangle + \frac{\mu}{2} \|\nabla u_{k+1}\|_2^2 + \|w_{k+1}\|_1 - \alpha \|w_{k+1}\|_{2,1} \\ &\quad + \frac{\beta_{k+1}}{2} \left\| Au_{k+1} - v_{k+1} + \frac{y_{k+1}}{\beta_{k+1}} \right\|_2^2 - \frac{\|y_{k+1}\|_2^2}{2\beta_{k+1}} \\ &\quad + \frac{\beta_{k+1}}{2} \left\| \nabla u_{k+1} - w_{k+1} + \frac{z_{k+1}}{\beta_{k+1}} \right\|_2^2 - \frac{\|z_{k+1}\|_2^2}{2\beta_{k+1}}. \end{aligned} \quad (39)$$

Combining (38) and (39), we have

$$\begin{aligned} \lambda \langle f - f \log f, \mathbb{1} \rangle + (1 - \alpha) \|w_{k+1}\|_1 - \frac{C_2}{\beta_0} &\leq \mathcal{L}_{\beta_{k+1}}(u_{k+1}, v_{k+1}, w_{k+1}, y_{k+1}, z_{k+1}) \\ &\leq \mathcal{L}_{\beta_0}(u_0, v_0, w_0, y_0, z_0) + \frac{2C_1}{\beta_0} \sum_{i=0}^k \frac{1}{\sigma^{i-1}} \\ &\quad - \frac{\nu}{2} \sum_{i=0}^k \|u_{i+1} - u_i\|_2^2 - \frac{\beta_0}{2} \sum_{i=0}^k \|v_{i+1} - v_i\|_2^2 \\ &\leq \mathcal{L}_{\beta_0}(u_0, v_0, w_0, y_0, z_0) + \frac{2C_1}{\beta_0} \sum_{i=0}^{\infty} \frac{1}{\sigma^{i-1}}. \end{aligned} \quad (40)$$

Since $\sigma > 1$, the infinite sum is finite, and hence we have $\forall k \in \mathbb{N}$,

$$\|w_{k+1}\|_1 \leq \frac{1}{1 - \alpha} \left(\mathcal{L}_{\beta_0}(u_0, v_0, w_0, y_0, z_0) - \lambda \langle f - f \log f, \mathbb{1} \rangle + \frac{2C_1}{\beta_0} \sum_{i=0}^{\infty} \frac{1}{\sigma^{i-1}} + \frac{C_2}{\beta_0} \right) < \infty,$$

which implies that $\{w_k\}_{k=1}^{\infty}$ is bounded. Also from (38) and (39), we have

$$\begin{aligned} \lambda \langle f - f \log f, \mathbb{1} \rangle - \frac{C_2}{\beta_0} &\leq \lambda \langle v_{k+1} - f \log v_{k+1}, \mathbb{1} \rangle - \frac{C_2}{\beta_0} \\ &\leq \lambda \langle v_{k+1} - f \log v_{k+1}, \mathbb{1} \rangle - \frac{\|y_{k+1}\|_2^2}{2\beta_{k+1}} - \frac{\|z_{k+1}\|_2^2}{2\beta_{k+1}} \\ &\leq \mathcal{L}_{\beta_{k+1}}(u_{k+1}, v_{k+1}, w_{k+1}, y_{k+1}, z_{k+1}) \\ &\leq \mathcal{L}_{\beta_0}(u_0, v_0, w_0, y_0, z_0) + \frac{2C_1}{\beta_0} \sum_{i=0}^{\infty} \frac{1}{\sigma^{i-1}} < \infty. \end{aligned}$$

This shows that $\{\langle v_k - f \log v_k, \mathbb{1} \rangle\}_{k=1}^{\infty}$ is bounded. By emulating the computation in (18), it can be shown that $\{v_k\}_{k=1}^{\infty}$ is bounded.

It suffices to prove that $\{(Au_k, \nabla u_k)\}_{k=1}^{\infty}$ is bounded in order to prove the boundedness of $\{u_k\}_{k=1}^{\infty}$ by Proposition 3. Using (21d), we have

$$\|Au_{k+1}\|_2 \leq \frac{\|y_{k+1} - y_k\|_2}{\beta_k} + \|v_{k+1}\|_2 \leq \frac{\sqrt{C_1}}{\beta_0} + \|v_{k+1}\|_2.$$

As $\{v_k\}_{k=1}^{\infty}$ is proven to be bounded, then $\{Au_k\}_{k=1}^{\infty}$ is also bounded. We can prove $\{\nabla u_k\}_{k=1}^{\infty}$ is bounded similarly using (21e). Altogether, $\{(u_k, v_k, w_k, y_k, z_k)\}_{k=1}^{\infty}$ is bounded.

It follows from (40) that

$$\begin{aligned} \frac{\nu}{2} \sum_{i=0}^k \|u_{i+1} - u_i\|_2^2 + \frac{\beta_0}{2} \sum_{i=0}^k \|v_{i+1} - v_i\|_2^2 &\leq \mathcal{L}_{\beta_0}(u_0, v_0, w_0, y_0, z_0) \\ &+ \frac{2C_1}{\beta_0} \sum_{i=0}^k \frac{1}{\sigma^{i-1}} - \lambda \langle f - f \log f, \mathbb{1} \rangle + \frac{C_2}{\beta_0}. \end{aligned}$$

As $k \rightarrow \infty$, we see the right-hand side is finite, which forces the infinite summations on the left-hand side to converge, and hence we have $u_{k+1} - u_k \rightarrow 0$ and $v_{k+1} - v_k \rightarrow 0$. \square

Theorem 9. *Suppose that $\ker(A) \cap \ker(\nabla) = \{0\}$ and $0 \leq \alpha < 1$. Let $\{(u_k, v_k, w_k, y_k, z_k)\}_{k=1}^\infty$ be generated by Algorithm 2. If $\{y_k\}_{k=1}^\infty$ bounded, $\beta_k(v_{k+1} - v_k) \rightarrow 0$, $\beta_k(w_{k+1} - w_k) \rightarrow 0$, $y_{k+1} - y_k \rightarrow 0$, and $z_{k+1} - z_k \rightarrow 0$, then there exists a subsequence whose limit point $(u^*, v^*, w^*, y^*, z^*)$ is a stationary point of (19) that satisfies the following:*

$$0 = -\mu \Delta u^* + A^\top y^* + \nabla^\top z^*, \quad (41a)$$

$$0 = \lambda \left(\mathbb{1} - \frac{f}{v^*} \right) - y^*, \quad (41b)$$

$$z^* \in \partial(\|w^*\|_1 - \alpha \|w^*\|_{2,1}), \quad (41c)$$

$$A u^* = v^*, \quad (41d)$$

$$\nabla u^* = w^*. \quad (41e)$$

Proof. By Lemma 8, the sequence $\{(u_k, v_k, w_k, y_k, z_k)\}_{k=1}^\infty$ is bounded, so there exists a subsequence $\{(u_{k_n}, v_{k_n}, w_{k_n}, y_{k_n}, z_{k_n})\}_{n=1}^\infty$ that converges to a point $(u^*, v^*, w^*, y^*, z^*)$. Additionally, we have $u_{k+1} - u_k \rightarrow 0$ and $v_{k+1} - v_k \rightarrow 0$. Since $\{(y_k, z_k)\}_{k=1}^\infty$ is bounded, there exists a constant $C > 0$ such that $\|y_{k+1} - y_k\|_2 < C$ and $\|z_{k+1} - z_k\|_2 < C$ for each $k \in \mathbb{N}$. By (21e), we have

$$\begin{aligned} \|w_{k+1} - w_k\|_2 &\leq \|w_{k+1} - \nabla u_{k+1}\|_2 + \|\nabla u_{k+1} - \nabla u_k\|_2 + \|\nabla u_k - w_k\|_2 \\ &= \frac{\|z_{k+1} - z_k\|_2}{\beta_k} + \|\nabla u_{k+1} - \nabla u_k\|_2 + \frac{\|z_k - z_{k-1}\|_2}{\beta_{k-1}} \\ &\leq \frac{2C}{\beta_{k-1}} + \|\nabla u_{k+1} - \nabla u_k\|_2. \end{aligned}$$

As $k \rightarrow \infty$, we have $w_{k+1} - w_k \rightarrow 0$. Altogether, we can derive the following results:

$$\lim_{n \rightarrow \infty} (u_{k_n+1}, v_{k_n+1}, w_{k_n+1}) = \lim_{n \rightarrow \infty} (u_{k_n}, v_{k_n}, w_{k_n}) = (u^*, v^*, w^*). \quad (42)$$

Furthermore, the assumptions give us

$$\begin{aligned} \lim_{n \rightarrow \infty} \beta_{k_n} (v_{k_n+1} - v_{k_n}) &= 0, \\ \lim_{n \rightarrow \infty} \beta_{k_n} (w_{k_n+1} - w_{k_n}) &= 0, \\ \lim_{n \rightarrow \infty} y_{k_n+1} - y_{k_n} &= 0, \\ \lim_{n \rightarrow \infty} z_{k_n+1} - z_{k_n} &= 0. \end{aligned}$$

By (21d)-(21e), we have

$$\begin{aligned}\|Au^* - v^*\|_2 &= \lim_{n \rightarrow \infty} \|Au_{k_n+1} - v_{k_n+1}\|_2 = \lim_{n \rightarrow \infty} \frac{\|y_{k_n+1} - y_{k_n}\|_2}{\beta_{k_n}} \leq \lim_{n \rightarrow \infty} \frac{C}{\beta_{k_n}} = 0, \\ \|\nabla u^* - w^*\|_2 &= \lim_{n \rightarrow \infty} \|\nabla u_{k_n+1} - w_{k_n+1}\|_2 = \lim_{n \rightarrow \infty} \frac{\|z_{k_n+1} - z_{k_n}\|_2}{\beta_{k_n}} \leq \lim_{n \rightarrow \infty} \frac{C}{\beta_{k_n}} = 0.\end{aligned}$$

Hence, we have $Au^* = v^*$ and $\nabla u^* = w^*$.

The optimality conditions at iteration k_n are the following:

$$-\mu \Delta u_{k_n+1} + A^\top y_{k_n} + \beta_{k_n} A^\top (Au_{k_n+1} - v_{k_n}) + \nabla^\top z_{k_n} + \beta_{k_n} \nabla^\top (\nabla u_{k_n+1} - w_{k_n}) = 0, \quad (43a)$$

$$\lambda \left(\mathbb{1} - \frac{f}{v_{k_n+1}} \right) - y_{k_n} - \beta_{k_n} (Au_{k_n+1} - v_{k_n+1}) = 0, \quad (43b)$$

$$z_{k_n} + \beta_{k_n} (\nabla u_{k_n+1} - w_{k_n+1}) \in \partial(\|w_{k_n+1}\|_1 - \alpha \|w_{k_n+1}\|_{2,1}). \quad (43c)$$

Expanding (43a) by substituting in (21d)-(21e) and taking the limit, we have

$$\begin{aligned}0 &= \lim_{n \rightarrow \infty} -\mu \Delta u_{k_n+1} + A^\top y_{k_n} + \beta_{k_n} A^\top (Au_{k_n+1} - v_{k_n}) + \nabla^\top z_{k_n} + \beta_{k_n} \nabla^\top (\nabla u_{k_n+1} - w_{k_n}) \\ &= \lim_{n \rightarrow \infty} -\mu \Delta u_{k_n+1} + A^\top y_{k_n} + \beta_{k_n} A^\top (Au_{k_n+1} - v_{k_n+1}) + \beta_{k_n} A^\top (v_{k_n+1} - v_{k_n}) + \nabla^\top z_{k_n} \\ &\quad + \beta_{k_n} \nabla^\top (\nabla u_{k_n+1} - w_{k_n+1}) + \beta_{k_n} \nabla^\top (w_{k_n+1} - w_{k_n}) \\ &= \lim_{n \rightarrow \infty} -\mu \Delta u_{k_n+1} + A^\top y_{k_n} + A^\top (y_{k_n+1} - y_{k_n}) + \beta_{k_n} A^\top (v_{k_n+1} - v_{k_n}) + \nabla^\top z_{k_n} \\ &\quad + \nabla^\top (z_{k_n+1} - z_{k_n}) + \beta_{k_n} \nabla^\top (w_{k_n+1} - w_{k_n}) \\ &= -\mu \Delta u^* + A^\top y^* + \nabla^\top z^*.\end{aligned}$$

Substituting in (21d) into (43b) and taking the limit give us

$$\begin{aligned}0 &= \lim_{n \rightarrow \infty} \lambda \left(\mathbb{1} - \frac{f}{v_{k_n+1}} \right) - y_{k_n} - \beta_{k_n} (Au_{k_n+1} - v_{k_n+1}) \\ &= \lim_{n \rightarrow \infty} \lambda \left(\mathbb{1} - \frac{f}{v_{k_n+1}} \right) - y_{k_n} - (y_{k_n+1} - y_{k_n}) \\ &= \lambda \left(\mathbb{1} - \frac{f}{v^*} \right) - y^*.\end{aligned}$$

Lastly, by substituting (21e) into (43c), we have

$$z_{k_n+1} \in \partial(\|w_{k_n+1}\|_1 - \alpha \|w_{k_n+1}\|_{2,1}).$$

By continuity, we have $\|w_{k_n+1}\|_1 - \alpha \|w_{k_n+1}\|_{2,1} \rightarrow \|w^*\|_1 - \alpha \|w^*\|_{2,1}$. Together with the fact that $(w_{k_n+1}, z_{k_n+1}) \rightarrow (w^*, z^*)$, we have $z^* \in \partial(\|w^*\|_1 - \alpha \|w^*\|_{2,1})$ by closedness of the subdifferential.

Therefore, $(u^*, v^*, w^*, y^*, z^*)$ is a stationary point. \square

Remark 2. *It is true that the assumptions in Theorem 9 are rather strong, but they are standard in the convergence analyses of other ADMM algorithms for nonconvex problems that fail to satisfy the conditions for global convergence in [69]. For example, [34, 35, 39, 43] assumed convergence of the successive differences of the primal variables and Lagrange multipliers. Instead, we modify the convergence of the successive difference*

of the primal variables, i.e., $\beta_k(v_{k+1} - v_k) \rightarrow 0, \beta_k(w_{k+1} - w_k) \rightarrow 0$. Boundedness of the Lagrange multiplier (i.e., $\{y_k\}_{k=1}^{\infty}$) was also assumed in [44, 76], which required a stronger assumption than ours regarding the successive difference of the Lagrange multipliers.

4 Numerical Experiments

In this section, we apply the proposed method of AITV Poisson SaT/SLaT on various grayscale and color images for image segmentation. For grayscale images, we compare our method with the original TV SaT [16], thresholded-Rudin-Osher-Fatemi (T-ROF) [11], and the Potts model [55] solved by either Pock’s algorithm (Pock) [54] or Storath and Weinmann’s algorithm (Storath) [60]. For color images, we compare with TV SLaT [10], Pock’s method [54], and Storath’s method [60]. We can solve (9) for TV SaT/SLaT via Algorithm 2 that utilizes the proximal operator corresponding to the $\|\cdot\|_{2,1}$ norm. The code for T-ROF is provided by the respective author¹ and we can adapt it to handle blur by using a more general data fidelity term. Pock’s method is implemented by the lab group². Storath’s method is provided by the original author³. Note that T-ROF, Pock’s method, and Storath’s method are designed for images corrupted with Gaussian noise. We apply the Anscombe transform [2] to the test images, after which the Poisson noise becomes approximately Gaussian noise. Since Storath’s method is not for segmentation, we perform a post-processing step of k -means clustering to its piecewise-constant output. For the SLaT methods, we parallelize the smoothing step separately for each channel.

To quantitatively measure the segmentation performance, we use the DICE index [24] and peak signal-to-noise ratio (PSNR). Let $S \subset \Omega$ be the ground-truth region and $S' \subset \Omega$ be a region obtained from the segmentation algorithm corresponding to the ground-truth region S . The DICE index is formulated by

$$\text{DICE} = \frac{2|S \cap S'|}{|S| + |S'|}.$$

To compare the piecewise-constant reconstruction \tilde{f} according to (10) with the original test image f , we compute PSNR by

$$\text{PSNR} = 20 \log_{10} \frac{(M \times N) \times P}{\sum_{i,j} (f_{i,j} - \tilde{f}_{i,j})^2},$$

where $M \times N$ is the image size and $P = \max_{i,j} f_{i,j}$.

Poisson noise is added to the test images by the MATLAB command `poissrnd`. To ease parameter tuning, we scale each test image to $[0, 1]$ after its degradation with Poisson noise and/or blur. We set $\sigma = 1.25$ and $\beta_{1,0} = \beta_{2,0} = 1.0, 2.0$ in Algorithm 2 for grayscale and color images, respectively. The stopping criterion is either 300 iterations or when the relative error of u_k is below $\epsilon = 10^{-4}$. We tune the fidelity parameter λ and the smoothing parameter μ for each image, which will be specified later. For T-ROF, Pock’s method, and Storath’s method, their parameters are manually tuned to give the best DICE indices for binary segmentation (Section 4.1) and the PSNR values for multiphase segmentation (Section 4.2-4.3). All experiments are performed in MATLAB R2022b on a Dell laptop with a 1.80 GHz Intel Core i7-8565U processor and 16.0 GB RAM.

¹<https://xiaohaocai.netlify.app/download/>

²Python code is available at <https://github.com/VLOGroup/pgmo-lecture/blob/master/notebooks/tv-potts.ipynb> and a translated MATLAB code is available at https://github.com/kbui1993/MATLAB_Potts.

³<https://github.com/mstorath/Pottslab>

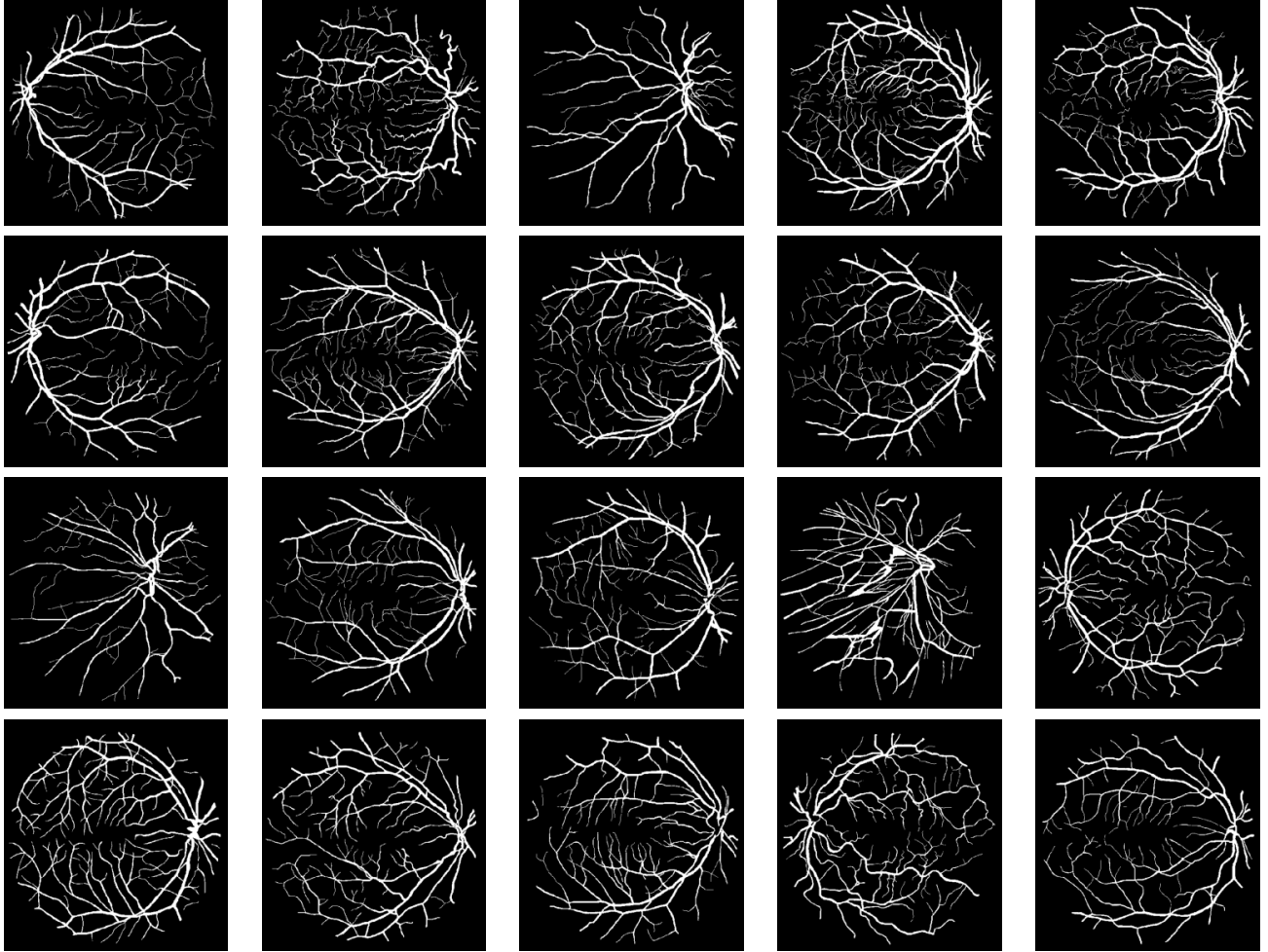


Figure 1: The entire DRIVE dataset [59] for binary segmentation. The image size is 584×565 with background value of 200 and the pixel value for vessels to be 255.

4.1 Grayscale, Binary Segmentation

We start with performing binary segmentation on the entire DRIVE dataset [59] that consists of 20 images shown in Figure 1. Each image has size 584×565 with modified pixel values of either 200 for the background or 255 for the vessels. Before adding Poisson noise, we set the peak value of the image to be $P/2$ or $P/5$, where $P = 255$. Note that a lower peak value indicates stronger noise in the image, thus more challenging for denoising. We examine three cases: (1) $P/2$ no blur, (2) $P/5$ no blur, and (3) $P/2$ with Gaussian blur specified by MATLAB command `fspecial('gaussian', [10 10], 2)`. For the TV SaT method, we set $\lambda = 14.5$, $\mu = 0.5$ for case (1), $\lambda = 8.0$, $\mu = 0.5$ for case (2), and $\lambda = 22.5$, $\mu = 0.25$ for case (3). For the AITV SaT method, the parameters λ and μ are set the same as TV SaT, and we have $\alpha = 0.3$ for cases (1)-(2) and $\alpha = 0.8$ for case (3).

Table 1 records the DICE indices and the computational time in seconds for the competing methods, averaged over 20 images. We observe that AITV SaT attains the best DICE indices for all three cases with comparable computational time to TV SaT and T-ROF, all of which are much faster than Pock and Storath. As visually illustrated in Figure 2, AITV SaT segments more of the thinner vessels compared to TV SaT and T-ROF in five images, thereby having the higher average DICE indices.

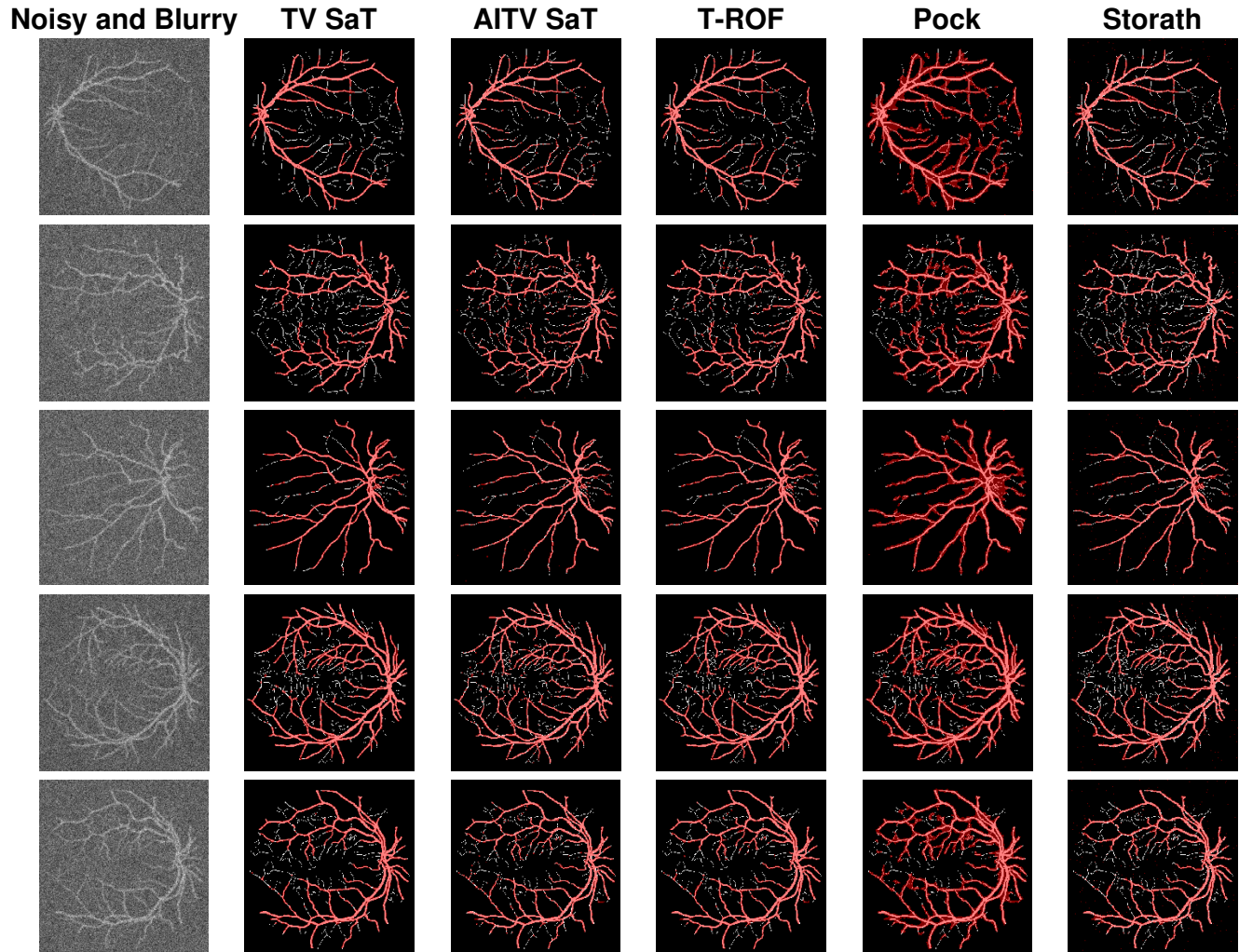


Figure 2: Binary segmentation results of Figure 1 with peak $P/2$ under Gaussian blur and Poisson noise.

Table 1: DICE and computational time in seconds of the binary segmentation methods averaged over 20 images in Figure 1 with standard deviations in parentheses. **Bold** indicates best result.

		TV SaT	AITV SaT	T-ROF	Pock	Storath
$P/2$ no blur	DICE	0.9464 (0.0091)	0.9501 (0.0076)	0.9463 (0.0073)	0.8466 (0.0301)	0.8855 (0.0181)
	Time (sec.)	4.2401 (0.3618)	5.7342 (0.5251)	4.9206 (1.4281)	24.7376 (3.2454)	19.9456 (1.8875)
$P/5$ no blur	DICE	0.8714 (0.0134)	0.8735 (0.0125)	0.8570 (0.0170)	0.6504 (0.0910)	0.8277 (0.0191)
	Time (sec.)	4.7076 (0.6937)	6.4027 (0.8441)	5.4943 (0.7935)	46.9346 (9.4969)	21.8734 (2.7660)
$P/2$ with Gaussian Blur	DICE	0.7244 (0.0254)	0.7411 (0.0220)	0.7322 (0.0251)	0.5473 (0.0398)	0.6944 (0.0217)
	Time (sec.)	7.4495 (1.0983)	9.2523 (1.5959)	11.7337 (2.1252)	47.3911 (10.9191)	19.9444 (2.4142)

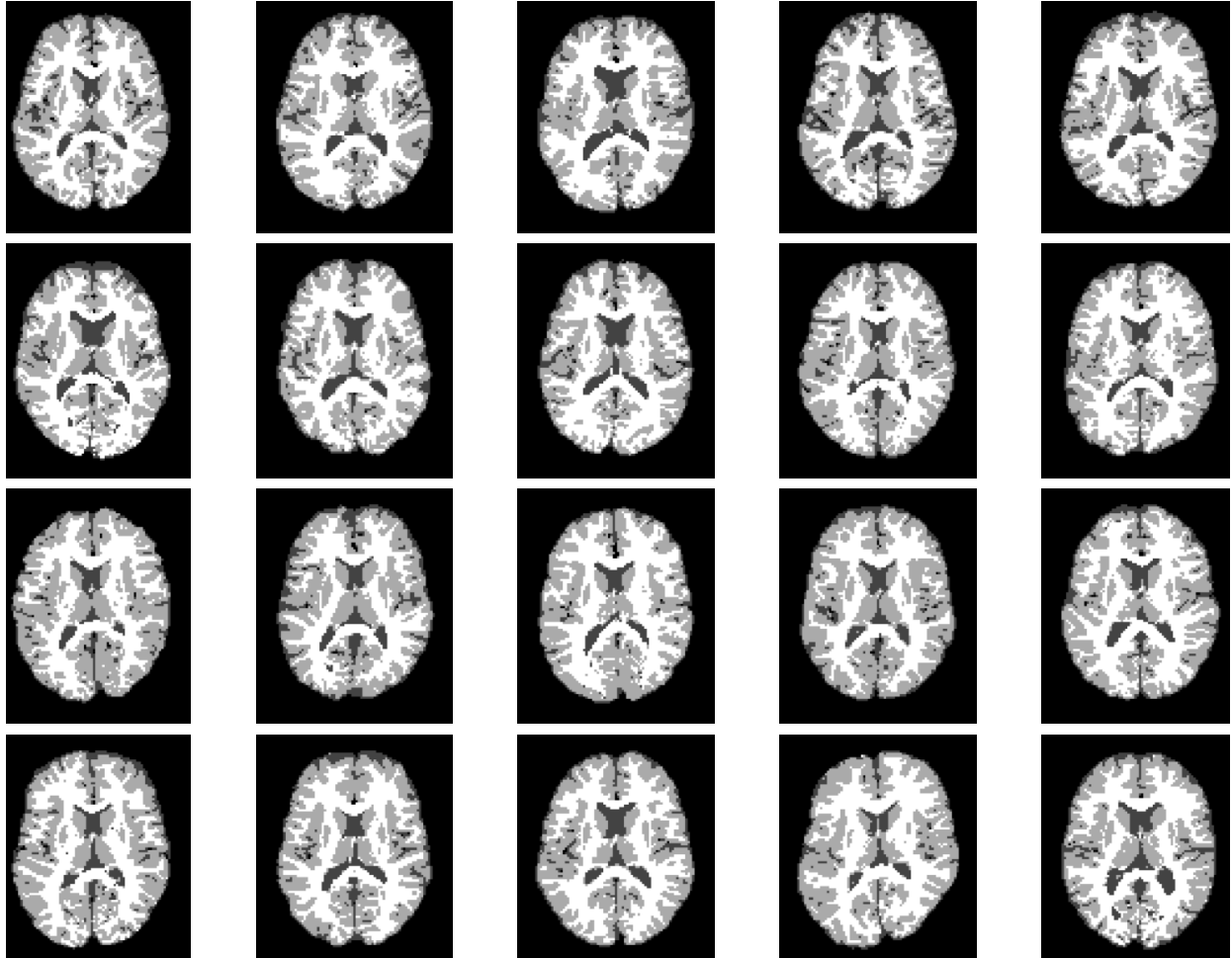


Figure 3: The entire BrainWeb dataset [3] for grayscale, multiphase segmentation. Each image is of size 104×87 . The pixel values are 10 (background), 48 (cerebrospinal fluid), 106 (grey matter), and 154 (white matter).

4.2 Grayscale, Multiphase Segmentation

We examine the multiphase segmentation on the entire BrainWeb dataset [3] that consists of 20 grayscale images as shown in Figure 3. Each image is of size 104×87 and has four regions to segment: background, cerebrospinal fluid (CSF), grey matter (GM), and white matter (WM). The pixel values are 10 (background), 48 (CSF), 106 (GM), and 154 (WM). The maximum intensity $P = 154$. We consider two cases: (1) $P/2$ no blur and (2) $P/2$ with motion blur specified by `fspecial('motion', 5, 225)`. For the SaT methods, we have $\mu = 1.0$, $\alpha = 0.6, 0.7$, and $\lambda = 4.0, 5.0$ for case (1) and case (2), respectively.

Across all 20 images of the BrainWeb dataset, Table 2 reports the average DICE indices for CSF, GM, and WM and average computational times in seconds of the segmentation methods. For both cases (1) and (2), AITV SaT attains the highest average DICE indices for segmenting CSF, GM, and WM. AITV SaT is comparable to TV SaT and T-ROF in terms of computational time.

Figure 4 shows the segmentation results of the first image in Figure 3 for case (1). When segmenting CSF, the methods (TV SaT, AITV SaT, and Storath) yield similar visual results, while Pock fails to segment roughly half of the region. In addition, AITV SaT segments the most GM region with the least amount of

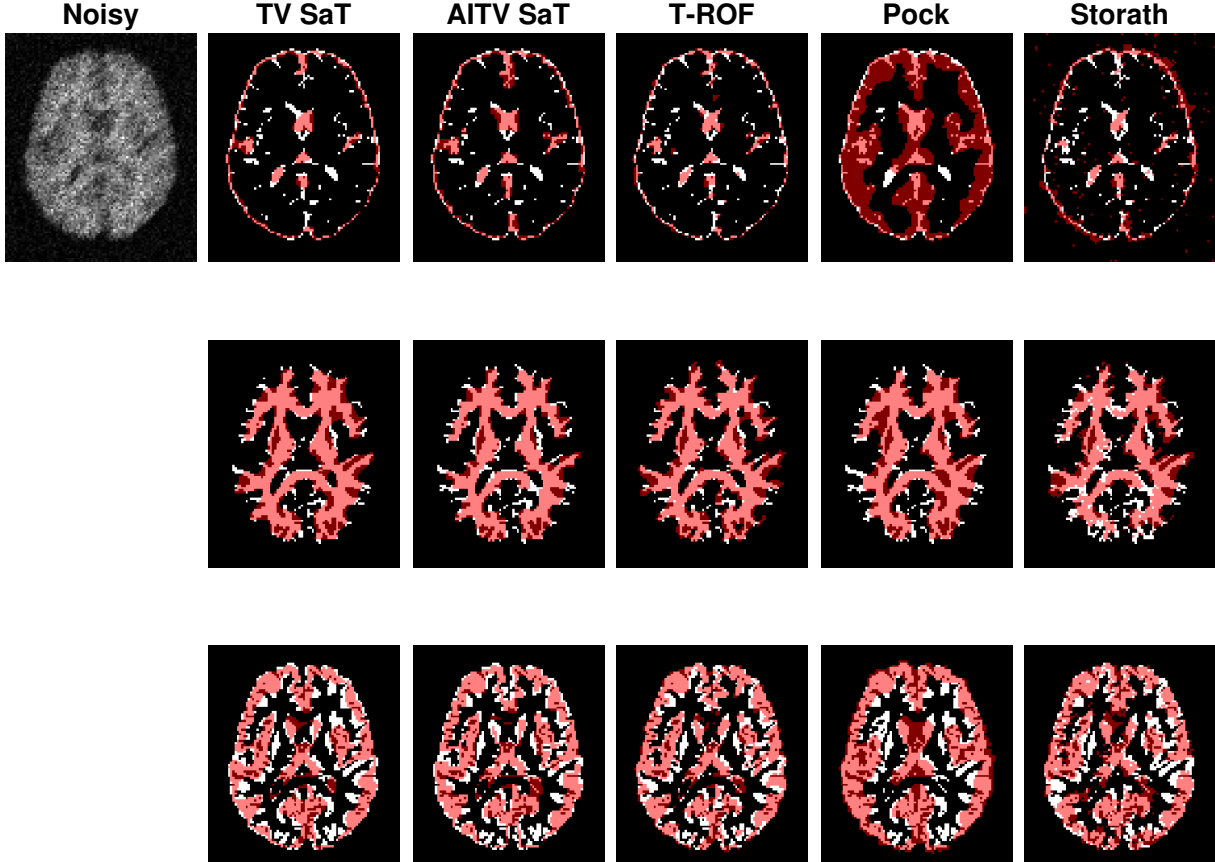


Figure 4: Segmentation result of the first image of Figure 3 with peak $P/8$ under Poisson noise with no blur. From top to bottom are segmentation results for CSF, GM, and WM.

Table 2: DICE and computational time in seconds of the multiphase segmentation methods averaged over 20 images in Figure 3 with standard deviations in parentheses. **Bold** indicates best result.

		TV SaT	AITV SaT	T-ROF	Pock	Storath
$P/8$ no blur	CSF DICE	0.8208 (0.0270)	0.8396 (0.0262)	0.7398 (0.1316)	0.4572 (0.1474)	0.8041 (0.0244)
	GM DICE	0.8097 (0.0258)	0.8477 (0.0157)	0.7904 (0.0422)	0.7507 (0.0719)	0.7900 (0.0344)
	WM DICE	0.8449 (0.0125)	0.8694 (0.0101)	0.8221 (0.0132)	0.8459 (0.0283)	0.8138 (0.0196)
	Time (sec.)	0.2607 (0.0625)	0.2863 (0.0470)	0.2202 (0.0324)	2.6139 (0.6690)	0.3383 (0.0948)
$P/8$ with Motion Blur	CSF DICE	0.6196 (0.0385)	0.6260 (0.0483)	0.6174 (0.0460)	0.3772 (0.0561)	0.4964 (0.0468)
	GM DICE	0.6809 (0.0304)	0.7138 (0.0262)	0.6528 (0.0358)	0.6345 (0.0590)	0.6544 (0.0399)
	WM DICE	0.7757 (0.0127)	0.7935 (0.0110)	0.7686 (0.0164)	0.7529 (0.0185)	0.7382 (0.0140)
	Time (sec.)	0.2494 (0.0443)	0.2854 (0.0279)	0.3647 (0.0693)	2.5782 (0.4683)	0.3052 (0.1399)

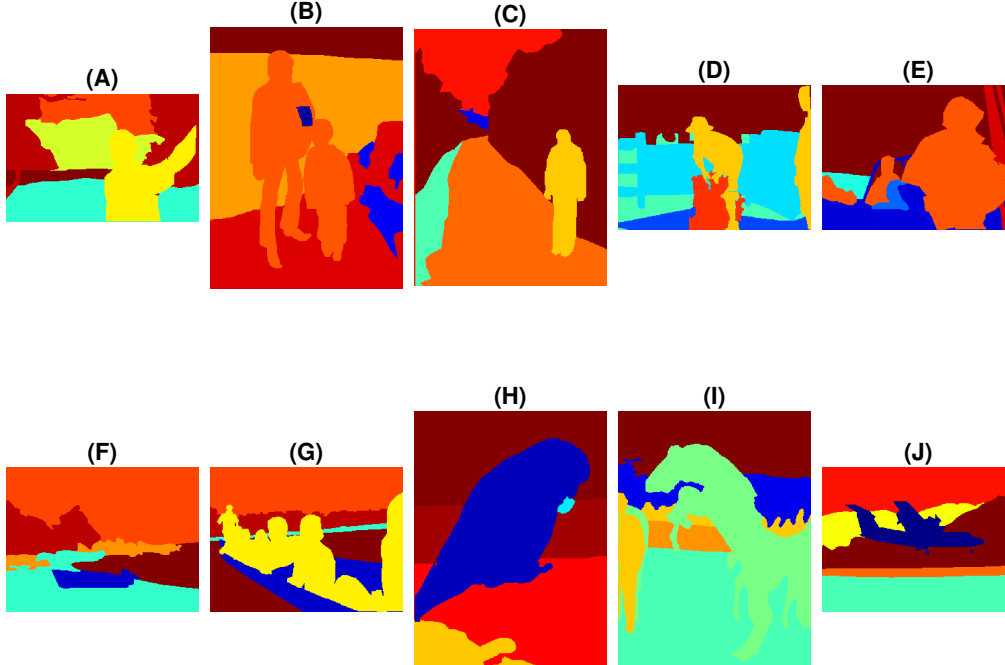


Figure 5: Test images from the PASCAL VOC 2010 dataset [28] for color, multiphase segmentation. Each image has 6 regions. The image sizes are (A) 307×461 , (B) 500×367 , (C) 500×375 , (D)-(G) 375×500 , (H)-(I) 500×375 , and (J) 375×500 .

noise artifacts than the other methods. Lastly, for WM segmentation, AITV SaT avoids the “holes” or “gaps” and segments fewer regions outside of the ground truth, thus outperforming TV SaT and Storath. For the three regions, T-ROF has the most noise artifacts in its segmentation results.

4.3 Color Segmentation

We perform color image segmentation on 10 images shown in Figure 5, which are selected from the PASCAL VOC 2010 dataset [28]. Each image has six different color regions. Figure 5(A) is of size 307×461 ; Figure 5(B) is of 500×367 ; Figures 5(C) and 5(H)-(I) are of 500×375 ; and Figures 5(D)-(G) and 5(J) are of 375×500 . Before adding Poisson noise to each channel of each image, we set the peak value $P = 10$. We choose the parameters of the SLaT methods to be $\lambda = 1.5$, $\mu = 0.05$, and $\alpha = 0.6$.

Figures 6-7 present the piecewise-constant approximations via (10), showing similar segmentation results obtained by TV SLaT, AITV SLaT, and Storath. Quantitatively in Table 3, AITV SLaT has better PSNRs than TV SLaT and Pock for all the images and outperforms Storath for seven. Overall, the proposed AITV SLaT has the highest PSNR on average over 10 images with the lowest standard deviation and comparable speed as Storath.

4.4 Parameter Analysis

The proposed smoothing model (11) involves the following parameters:

- *The fidelity parameter* λ weighs how close the approximation Au^* is to the original image f . For a larger amount of noise, the value of λ should be chosen smaller.

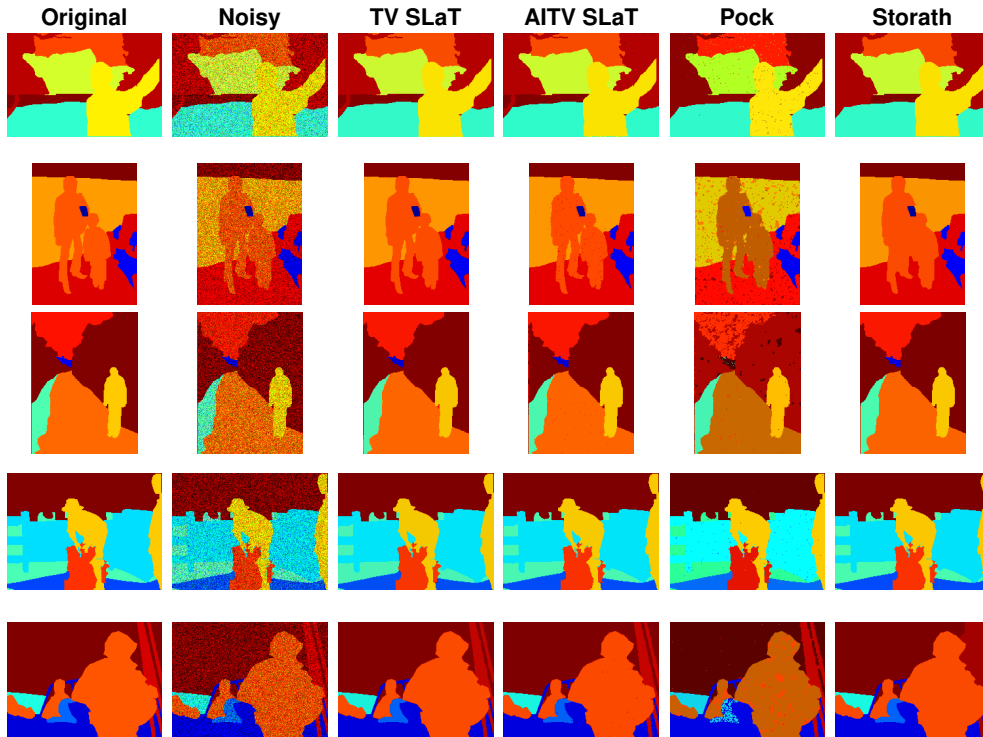


Figure 6: Color image segmentation results of Figures 5(A)-(E).

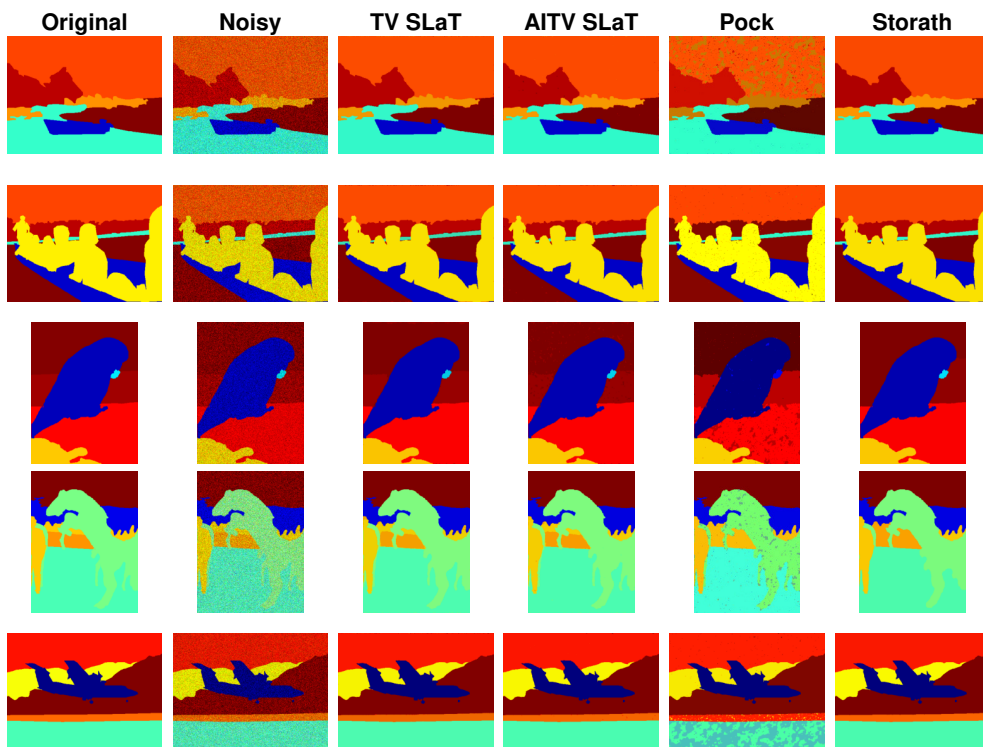


Figure 7: Color image segmentation results of Figures 5(F)-(J).

Table 3: PSNR and computation time in seconds for color image segmentation of the images in Figure 5. **Bold** indicates best result.

		TV SLaT	AITV SLaT	Pock	Storath
PSNR	Figure 5(A)	29.0337	30.4619	19.2306	28.7141
	Figure 5(B)	31.8673	31.7055	17.3512	30.9703
	Figure 5(C)	30.9605	33.4217	18.0389	32.2217
	Figure 5(D)	29.5265	32.5505	21.4873	34.7881
	Figure 5(E)	29.8903	31.0656	19.7646	28.3456
	Figure 5(F)	33.2308	34.7619	17.9788	34.4106
	Figure 5(G)	28.1136	30.6237	22.5048	31.2439
	Figure 5(H)	33.2682	33.4250	18.9390	31.9377
	Figure 5(I)	30.0659	31.7937	20.0856	29.3905
	Figure 5(J)	31.4164	34.0610	20.3185	34.3599
	Avg. (Std.)	30.7373 (1.7266)	32.3870 (1.4905)	19.5700 (1.6147)	31.6383 (2.3686)
Time (sec.)	Figure 5(A)	7.1992	8.2455	148.9232	4.9410
	Figure 5(B)	12.2238	11.8890	321.0637	9.9533
	Figure 5(C)	5.6775	7.4494	384.6998	10.1785
	Figure 5(D)	4.9511	7.2061	128.4236	7.0026
	Figure 5(E)	6.2380	7.0719	275.0501	7.9808
	Figure 5(F)	6.0509	7.2392	398.1339	10.0982
	Figure 5(G)	7.2821	7.6919	165.2142	7.9315
	Figure 5(H)	6.0269	9.7018	385.3311	7.9389
	Figure 5(I)	7.0375	8.0875	250.3698	9.7501
	Figure 5(J)	6.1873	10.6472	334.8662	7.2176
	Avg. (Std.)	6.8874 (2.0088)	8.5230 (1.6610)	279.2076 (102.7063)	8.2993 (1.7031)

- The smoothing parameter μ determines how smooth the solution u^* should be. A larger value of μ may improve denoising, but at a cost of smearing out the edges between adjacent regions, which may be segmented together if they have similar colors.
- The sparsity parameter $\alpha \in [0, 1]$ determines how sparse the gradient vector at each pixel should be. More specifically, the closer the value α is to 1, the more $\|\nabla u\|_1 - \alpha\|\nabla u\|_{2,1}$ resembles $\|\nabla u\|_0$.

We perform sensitivity analysis on these parameters to understand how they affect the segmentation quality of AITV SaT/SLaT. We consider two types of tests in the case of $P/8$ with motion blur in Figure 3. In the first case (Figure 8), we fix $\mu = 1.0$ and vary α, λ . In the second case (Figure 9), we fix $\lambda = 5.0$ and vary α, μ . Figure 8 reveals a concave relationship of the DICE index of each region with respect to the parameter λ , which implies there exists the optimal choice of λ . Additionally, when λ is small, a large value for α can improve the DICE indices. According to Figure 9, the DICE indices of the GM and WM regions decrease with respect to μ , while the DICE index of the CSF region is approximately constant. For $\alpha = 0.8$, the DICE indices of the GM and WM regions are the largest when $\mu \geq 1$, but the large α is not optimal for CSF. Hence, an intermediate value of α , such as 0.6, is preferable to attain satisfactory segmentation quality for all three regions.

Lastly, in Figure 10, we conduct sensitive analysis for the case of $P = 10$ of Figure 5. We fix $\mu = 0.05$, while varying λ, α in Figure 10(A), which indicates that the optimal value for α is in the range of $0.5 \leq \alpha \leq 0.7$. Then we fix $\lambda = 1.5$ to examine μ and α in Figure 10(B). For $0.2 \leq \alpha \leq 0.7$, PSNR decreases as μ increases. Again, $\alpha = 0.6$ generally yields the best PSNR.

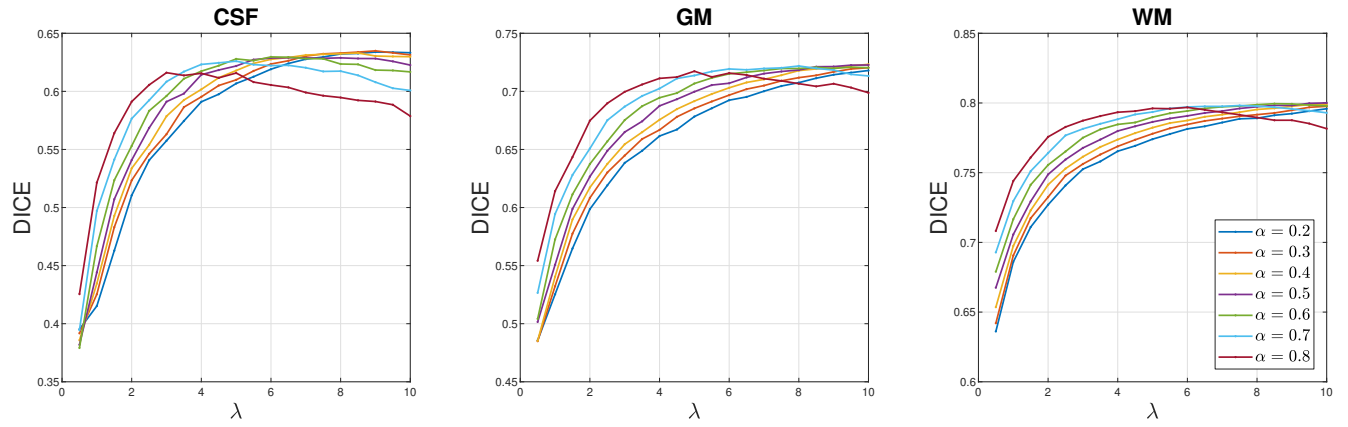


Figure 8: Sensitivity analysis on λ for the $P/8$ with motion blur case of Figure 3. The parameter $\mu = 1.0$ is fixed. DICE indices averaged over 10 images for each brain region are plotted with respect to λ .

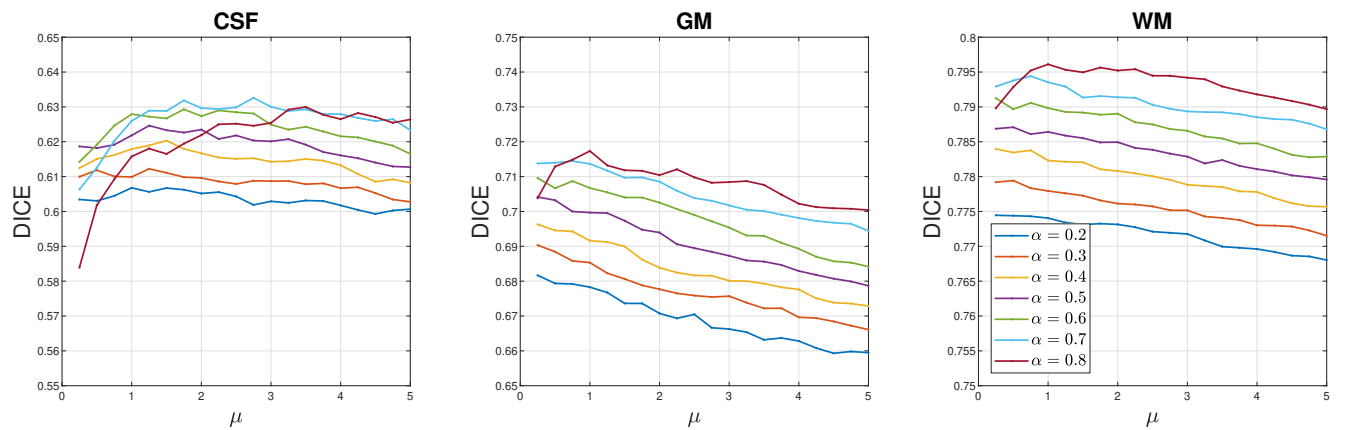


Figure 9: Sensitivity analysis on μ for the $P/8$ with motion blur case of Figure 3. The parameter $\lambda = 5.0$ is fixed. DICE indices averaged over 10 images for each brain region are plotted with respect to μ .

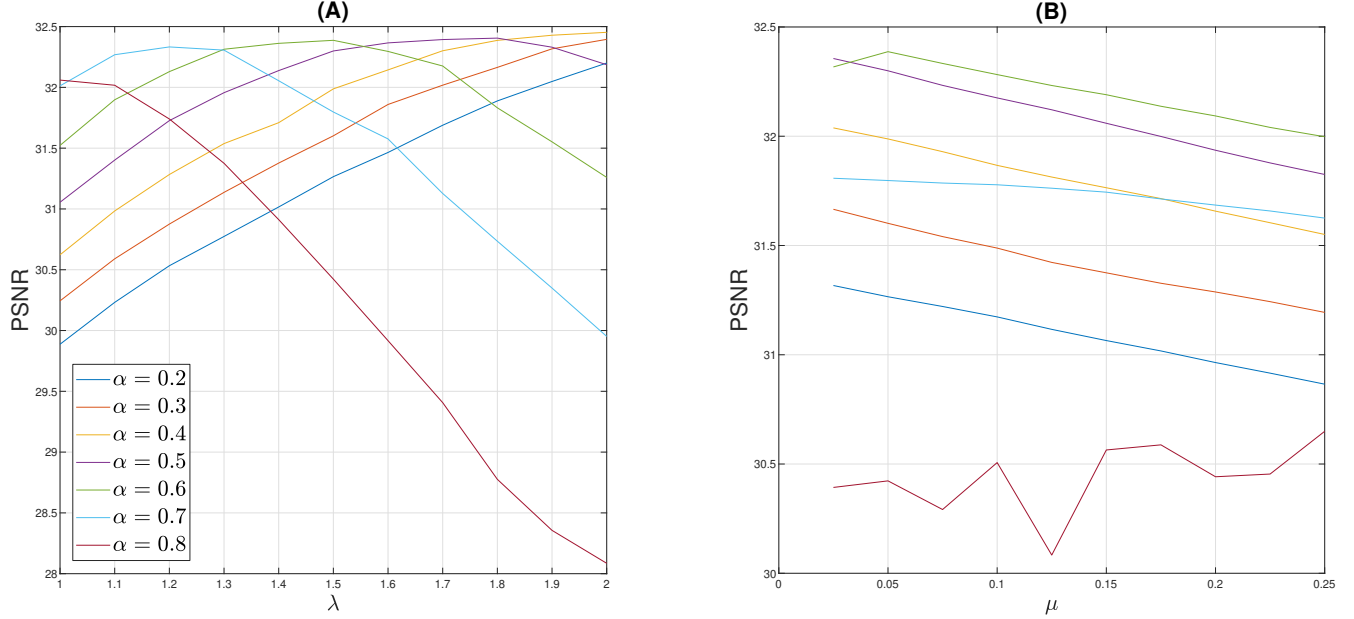


Figure 10: Sensitivity analysis of parameters for $P = 10$ case of Figure 5. (A) is the sensitivity analysis on λ when $\mu = 0.05$ fixed; (B) is the sensitivity analysis on μ when $\lambda = 1.5$ fixed. Average PSNR is plotted.

5 Conclusion and future work

In this paper, we developed the AITV Poisson SaT/SLaT framework for image segmentation. In particular, we proposed a simplified Mumford-Shah model with the AITV regularization and Poisson fidelity for the smoothing step. The model was proven to have a global minimizer. Our numerical algorithm incorporated a specific splitting scheme for ADMM and the $\ell_1 - \alpha\ell_2$ proximal operator for solving a subproblem. Convergence analysis established that the sequence generated by ADMM has a convergent subsequence to a stationary point of the nonconvex model. In our numerical experiments, the AITV Poisson SaT/SLaT yielded high-quality segmentation results within seconds for various grayscale and color images corrupted with Poisson noise and/or blur. For future directions, we are interested in other nonconvex regularization, such as ℓ_1/ℓ_2 on the gradient [65, 66, 72], ℓ_p , $0 < p < 1$, on the gradient [32, 43, 73], and transformed total variation [33], as alternatives to AITV. On the other hand, we can develop AITV variants of weighted TV [41] or adaptive TV [71, 80]. Moreover, we plan to determine how to make the sparsity parameter α in AITV adaptable to each image. In future work, we will adapt other segmentation algorithms [11, 34, 35, 38, 39, 52, 78] designed for Gaussian noise or impulsive noise to Poisson noise.

Conflict of Interest Statement

The authors declare that the research was conducted in the absence of any commercial or financial relationships that could be construed as a potential conflict of interest.

Author Contributions

KB performed the experiments and analysis and drafted the manuscript. All authors contributed to the design, evaluation, discussions and production of the manuscript.

Funding

The work was partially supported by NSF grants DMS-1846690, DMS-1854434, DMS-1952644, DMS-2151235, and a Qualcomm Faculty Award.

Data Availability Statement

The images in Figure 1 are provided from the DRIVE dataset [59] at <https://drive.grand-challenge.org/DRIVE/>. The images in Figure 3 are extracted from BrainWeb [3] via the Python package “brainweb” provided at <https://github.com/casperdcl/brainweb>. The images in Figure 5 are selected from the PASCAL VOC 2010 dataset [28]. Code for AITV Poisson SaT/SLaT is available at https://github.com/kbui1993/Official_Poisson_AITV_SaT_SLaT.

References

- [1] L. AMBROSIO AND V. M. TORTORELLI, *Approximation of functional depending on jumps by elliptic functional via t -convergence*, Communications on Pure and Applied Mathematics, 43 (1990), pp. 999–1036.
- [2] F. J. ANSCOMBE, *The transformation of Poisson, binomial and negative-binomial data*, Biometrika, 35 (1948), pp. 246–254.
- [3] B. AUBERT-BROCHE, M. GRIFFIN, G. B. PIKE, A. C. EVANS, AND D. L. COLLINS, *Twenty new digital brain phantoms for creation of validation image data bases*, IEEE Transactions on Medical Imaging, 25 (2006), pp. 1410–1416.
- [4] L. BAR, T. F. CHAN, G. CHUNG, M. JUNG, N. KIRYATI, R. MOHIEDDINE, N. SOCHEN, AND L. A. VESE, *Mumford and Shah model and its applications to image segmentation and image restoration*, in Handbook of Mathematical Methods in Imaging, Springer, 2011, pp. 1095–1157.
- [5] A. BECK, *First-order methods in optimization*, SIAM, 2017.
- [6] S. BOYD, N. PARIKH, E. CHU, B. PELEATO, J. ECKSTEIN, ET AL., *Distributed optimization and statistical learning via the alternating direction method of multipliers*, Foundations and Trends® in Machine Learning, 3 (2011), pp. 1–122.
- [7] K. BUI, J. FAUMAN, D. KES, L. TORRES MANDIOLA, A. CIOMAGA, R. SALAZAR, A. L. BERTOZZI, J. GILLES, D. P. GORONZY, A. I. GUTTENTAG, ET AL., *Segmentation of scanning tunneling microscopy images using variational methods and empirical wavelets*, Pattern Analysis and Applications, 23 (2020), pp. 625–651.
- [8] K. BUI, Y. LOU, F. PARK, AND J. XIN, *An efficient smoothing and thresholding image segmentation framework with weighted anisotropic-isotropic total variation*, arXiv preprint arXiv:2202.10115, (2022).

- [9] K. BUI, F. PARK, Y. LOU, AND J. XIN, *A weighted difference of anisotropic and isotropic total variation for relaxed Mumford–Shah color and multiphase image segmentation*, SIAM Journal on Imaging Sciences, 14 (2021), pp. 1078–1113.
- [10] X. CAI, R. CHAN, M. NIKOLOVA, AND T. ZENG, *A three-stage approach for segmenting degraded color images: Smoothing, lifting and thresholding (SLaT)*, Journal of Scientific Computing, 72 (2017), pp. 1313–1332.
- [11] X. CAI, R. CHAN, C.-B. SCHONLIEB, G. STEIDL, AND T. ZENG, *Linkage between piecewise constant Mumford–Shah model and Rudin–Osher–Fatemi model and its virtue in image segmentation*, SIAM Journal on Scientific Computing, 41 (2019), pp. B1310–B1340.
- [12] X. CAI, R. CHAN, AND T. ZENG, *A two-stage image segmentation method using a convex variant of the Mumford–Shah model and thresholding*, SIAM Journal on Imaging Sciences, 6 (2013), pp. 368–390.
- [13] W. CAO, J. SUN, AND Z. XU, *Fast image deconvolution using closed-form thresholding formulas of $L_q(q = \frac{1}{2}, \frac{2}{3})$ regularization*, Journal of Visual Communication and Image Representation, 24 (2013), pp. 31–41.
- [14] P. CASCARANO, L. CALATRONI, AND E. L. PICCOLOMINI, *Efficient ℓ^0 gradient-based super-resolution for simplified image segmentation*, IEEE Transactions on Computational Imaging, 7 (2021), pp. 399–408.
- [15] A. CHAMBOLLE AND T. POCK, *A first-order primal-dual algorithm for convex problems with applications to imaging*, Journal of mathematical imaging and vision, 40 (2011), pp. 120–145.
- [16] R. CHAN, H. YANG, AND T. ZENG, *A two-stage image segmentation method for blurry images with Poisson or multiplicative Gamma noise*, SIAM Journal on Imaging Sciences, 7 (2014), pp. 98–127.
- [17] T. F. CHAN, S. ESEDOGLU, AND M. NIKOLOVA, *Algorithms for finding global minimizers of image segmentation and denoising models*, SIAM Journal on Applied Mathematics, 66 (2006), pp. 1632–1648.
- [18] T. F. CHAN AND L. A. VESE, *Active contours without edges*, IEEE Transactions on Image Processing, 10 (2001), pp. 266–277.
- [19] H. CHANG, Y. LOU, Y. DUAN, AND S. MARCHESINI, *Total variation–based phase retrieval for Poisson noise removal*, SIAM Journal on Imaging Sciences, 11 (2018), pp. 24–55.
- [20] R. CHARTRAND, *Exact reconstruction of sparse signals via nonconvex minimization*, IEEE Signal Processing Letters, 14 (2007), pp. 707–710.
- [21] R. CHOKSI, Y. G. GENNIP, AND A. OBERMAN, *Anisotropic total variation regularized L^1 approximation and denoising/deblurring of 2D bar codes*, Inverse Problems & Imaging, 5 (2011), pp. 591–617.
- [22] M. R. CHOWDHURY, J. QIN, AND Y. LOU, *Non-blind and blind deconvolution under Poisson noise using fractional-order total variation*, Journal of Mathematical Imaging and Vision, 62 (2020), pp. 1238–1255.
- [23] M. R. CHOWDHURY, J. ZHANG, J. QIN, AND Y. LOU, *Poisson image denoising based on fractional-order total variation*, Inverse Problems & Imaging, 14 (2020).
- [24] L. R. DICE, *Measures of the amount of ecologic association between species*, Ecology, 26 (1945), pp. 297–302.

- [25] L. DING AND W. HAN, $\alpha\ell_1 - \beta\ell_2$ regularization for sparse recovery, *Inverse Problems*, 35 (2019), p. 125009.
- [26] Y. DUAN, H. CHANG, W. HUANG, J. ZHOU, Z. LU, AND C. WU, *The L_0 regularized Mumford–Shah model for bias correction and segmentation of medical images*, *IEEE Transactions on Image Processing*, 24 (2015), pp. 3927–3938.
- [27] L. C. EVANS, *Partial differential equations*, vol. 19, American Mathematical Soc., 2010.
- [28] M. EVERINGHAM, L. VAN GOOL, C. K. WILLIAMS, J. WINN, AND A. ZISSERMAN, *The PASCAL visual object classes (VOC) challenge*, *International Journal of Computer Vision*, 88 (2009), pp. 303–308.
- [29] H. GE AND P. LI, *The Dantzig selector: recovery of signal via $\ell_1 - \alpha\ell_2$ minimization*, *Inverse Problems*, 38 (2021), p. 015006.
- [30] S. GU, Q. XIE, D. MENG, W. ZUO, X. FENG, AND L. ZHANG, *Weighted nuclear norm minimization and its applications to low level vision*, *International Journal of Computer Vision*, 121 (2017), pp. 183–208.
- [31] W. GUO, Y. LOU, J. QIN, AND M. YAN, *A novel regularization based on the error function for sparse recovery*, *Journal of Scientific Computing*, 87 (2021), pp. 1–22.
- [32] M. HINTERMÜLLER AND T. WU, *Nonconvex TV^q -models in image restoration: Analysis and a trust-region regularization-based superlinearly convergent solver*, *SIAM Journal on Imaging Sciences*, 6 (2013), pp. 1385–1415.
- [33] L. HUO, W. CHEN, H. GE, AND M. K. NG, *Stable image reconstruction using transformed total variation minimization*, *SIAM Journal on Imaging Sciences*, 15 (2022), pp. 1104–1139.
- [34] M. JUNG, *Piecewise-smooth image segmentation models with l^1 data-fidelity terms*, *Journal of Scientific Computing*, 70 (2017), pp. 1229–1261.
- [35] M. JUNG, M. KANG, AND M. KANG, *Variational image segmentation models involving non-smooth data-fidelity terms*, *Journal of Scientific Computing*, 59 (2014), pp. 277–308.
- [36] H. LANTÉRI AND C. THEYS, *Restoration of astrophysical images—the case of Poisson data with additive Gaussian noise*, *EURASIP Journal on Advances in Signal Processing*, 2005 (2005), pp. 1–14.
- [37] T. LE, R. CHARTRAND, AND T. J. ASAKI, *A variational approach to reconstructing images corrupted by Poisson noise*, *Journal of Mathematical Imaging and Vision*, 27 (2007), pp. 257–263.
- [38] F. LI, M. K. NG, T. Y. ZENG, AND C. SHEN, *A multiphase image segmentation method based on fuzzy region competition*, *SIAM Journal on Imaging Sciences*, 3 (2010), pp. 277–299.
- [39] F. LI, S. OSHER, J. QIN, AND M. YAN, *A multiphase image segmentation based on fuzzy membership functions and $L1$ -norm fidelity*, *Journal of Scientific Computing*, 69 (2016), pp. 82–106.
- [40] H. LI, W. GUO, J. LIU, L. CUI, AND D. XIE, *Image segmentation with adaptive spatial priors from joint registration*, *SIAM Journal on Imaging Sciences*, 15 (2022), pp. 1314–1344.
- [41] M.-M. LI AND B.-Z. LI, *A novel weighted anisotropic total variational model for image applications*, *Signal, Image and Video Processing*, 16 (2022), pp. 211–218.

- [42] P. LI, W. CHEN, H. GE, AND M. K. NG, $\ell_1 - \alpha\ell_2$ minimization methods for signal and image reconstruction with impulsive noise removal, *Inverse Problems*, 36 (2020), p. 055009.
- [43] Y. LI, C. WU, AND Y. DUAN, *The TV_p regularized Mumford-Shah model for image labeling and segmentation*, *IEEE Transactions on Image Processing*, 29 (2020), pp. 7061–7075.
- [44] H. LIU, K. DENG, H. LIU, AND Z. WEN, *An entropy-regularized ADMM for binary quadratic programming*, *Journal of Global Optimization*, (2022), pp. 1–33.
- [45] Y. LOU, S. OSHER, AND J. XIN, *Computational aspects of constrained $L_1 - L_2$ minimization for compressive sensing*, in *Modelling, Computation and Optimization in Information Systems and Management Sciences*, Springer, 2015, pp. 169–180.
- [46] Y. LOU AND M. YAN, *Fast L_1 - L_2 minimization via a proximal operator*, *Journal of Scientific Computing*, 74 (2018), pp. 767–785.
- [47] Y. LOU, P. YIN, Q. HE, AND J. XIN, *Computing sparse representation in a highly coherent dictionary based on difference of L_1 and L_2* , *Journal of Scientific Computing*, 64 (2015), pp. 178–196.
- [48] Y. LOU, T. ZENG, S. OSHER, AND J. XIN, *A weighted difference of anisotropic and isotropic total variation model for image processing*, *SIAM Journal on Imaging Sciences*, 8 (2015), pp. 1798–1823.
- [49] Q.-T. LUONG, *Color in computer vision*, in *Handbook of Pattern Recognition and Computer Vision*, World Scientific, 1993, pp. 311–368.
- [50] D. B. MUMFORD AND J. SHAH, *Optimal approximations by piecewise smooth functions and associated variational problems*, *Communications on Pure and Applied Mathematics*, (1989).
- [51] S. OSHER AND J. A. SETHIAN, *Fronts propagating with curvature-dependent speed: Algorithms based on Hamilton-Jacobi formulations*, *Journal of Computational Physics*, 79 (1988), pp. 12–49.
- [52] Z.-F. PANG, M. GENG, L. ZHANG, Y. ZHOU, T. ZENG, L. ZHENG, N. ZHANG, D. LIANG, H. ZHENG, Y. DAI, ET AL., *Adaptive weighted curvature-based active contour for ultrasonic and 3T/5T MR image segmentation*, *Signal Processing*, 205 (2023), p. 108881.
- [53] F. PARK, Y. LOU, AND J. XIN, *A weighted difference of anisotropic and isotropic total variation for relaxed Mumford-Shah image segmentation*, in *2016 IEEE International Conference on Image Processing (ICIP)*, IEEE, 2016, pp. 4314–4318.
- [54] T. POCK, A. CHAMBOLLE, D. CREMERS, AND H. BISCHOF, *A convex relaxation approach for computing minimal partitions*, in *2009 IEEE Conference on Computer Vision and Pattern Recognition*, IEEE, 2009, pp. 810–817.
- [55] R. B. POTTS, *Some generalized order-disorder transformations*, *Mathematical Proceedings of the Cambridge Philosophical Society*, 48 (1952), p. 106–109.
- [56] Y. RAHIMI, C. WANG, H. DONG, AND Y. LOU, *A scale-invariant approach for sparse signal recovery*, *SIAM Journal of Scientific Computing*, 41 (2019), pp. A3649–A3672.
- [57] R. T. ROCKAFELLAR AND R. J.-B. WETS, *Variational analysis*, vol. 317, Springer Science & Business Media, 2009.

- [58] L. I. RUDIN, S. OSHER, AND E. FATEMI, *Nonlinear total variation based noise removal algorithms*, *Physica D: Nonlinear Phenomena*, 60 (1992), pp. 259–268.
- [59] J. STAAL, M. D. ABRÀMOFF, M. NIEMEIJER, M. A. VIERGEVER, AND B. VAN GINNEKEN, *Ridge-based vessel segmentation in color images of the retina*, *IEEE Transactions on Medical Imaging*, 23 (2004), pp. 501–509.
- [60] M. STORATH AND A. WEINMANN, *Fast partitioning of vector-valued images*, *SIAM Journal on Imaging Sciences*, 7 (2014), pp. 1826–1852.
- [61] M. STORATH, A. WEINMANN, AND L. DEMARET, *Jump-sparse and sparse recovery using Potts functionals*, *IEEE Transactions on Signal Processing*, 62 (2014), pp. 3654–3666.
- [62] S. TONGBRAM, B. A. SHIMRAY, L. S. SINGH, AND N. DHANACHANDRA, *A novel image segmentation approach using fcm and whale optimization algorithm*, *Journal of Ambient Intelligence and Humanized Computing*, (2021), pp. 1–15.
- [63] Y. VARDI, L. A. SHEPP, AND L. KAUFMAN, *A statistical model for positron emission tomography*, *Journal of the American Statistical Association*, 80 (1985), pp. 8–20.
- [64] L. A. VESE AND T. F. CHAN, *A multiphase level set framework for image segmentation using the Mumford and Shah model*, *International Journal of Computer Vision*, 50 (2002), pp. 271–293.
- [65] C. WANG, M. TAO, C.-N. CHUAH, J. NAGY, AND Y. LOU, *Minimizing l_1 over l_2 norms on the gradient*, *Inverse Problems*, 38 (2022), p. 065011.
- [66] C. WANG, M. TAO, J. G. NAGY, AND Y. LOU, *Limited-angle CT reconstruction via the l_1/l_2 minimization*, *SIAM Journal on Imaging Sciences*, 14 (2021), pp. 749–777.
- [67] C. WANG, M. YAN, Y. RAHIMI, AND Y. LOU, *Accelerated schemes for the l_1/l_2 minimization*, *IEEE Transaction on Signal Processing*, 68 (2020), pp. 2660–2669.
- [68] Y. WANG, J. YANG, W. YIN, AND Y. ZHANG, *A new alternating minimization algorithm for total variation image reconstruction*, *SIAM Journal on Imaging Sciences*, 1 (2008), pp. 248–272.
- [69] Y. WANG, W. YIN, AND J. ZENG, *Global convergence of ADMM in nonconvex nonsmooth optimization*, *Journal of Scientific Computing*, 78 (2019), pp. 29–63.
- [70] Y. WEN, R. H. CHAN, AND T. ZENG, *Primal-dual algorithms for total variation based image restoration under Poisson noise*, *Science China Mathematics*, 59 (2016), pp. 141–160.
- [71] T. WU, X. GU, Y. WANG, AND T. ZENG, *Adaptive total variation based image segmentation with semi-proximal alternating minimization*, *Signal Processing*, 183 (2021), p. 108017.
- [72] T. WU, Z. MAO, Z. LI, Y. ZENG, AND T. ZENG, *Efficient color image segmentation via quaternion-based L_1/L_2 regularization*, *Journal of Scientific Computing*, 93 (2022), p. 9.
- [73] T. WU, J. SHAO, X. GU, M. K. NG, AND T. ZENG, *Two-stage image segmentation based on nonconvex $l_2 - l_p$ approximation and thresholding*, *Applied Mathematics and Computation*, 403 (2021), p. 126168.
- [74] T. WU, Y. ZHAO, Z. MAO, L. SHI, Z. LI, AND Y. ZENG, *Image segmentation via Fischer-Burmeister total variation and thresholding*, *Advances in Applied Mathematics and Mechanics*, 14 (2022), pp. 960–988.

- [75] Y. XU, A. NARAYAN, H. TRAN, AND C. G. WEBSTER, *Analysis of the ratio of l_1 and l_2 norms in compressed sensing*, Applied and Computational Harmonic Analysis, 55 (2021), pp. 486–511.
- [76] Y. XU, W. YIN, Z. WEN, AND Y. ZHANG, *An alternating direction algorithm for matrix completion with nonnegative factors*, Frontiers of Mathematics in China, 7 (2012), pp. 365–384.
- [77] Z. XU, X. CHANG, F. XU, AND H. ZHANG, *$L_{1/2}$ regularization: A thresholding representation theory and a fast solver*, IEEE Transactions on Neural Networks and Learning Systems, 23 (2012), pp. 1013–1027.
- [78] J. YANG, Z. GUO, D. ZHANG, B. WU, AND S. DU, *An anisotropic diffusion system with nonlinear time-delay structure tensor for image enhancement and segmentation*, Computers & Mathematics with Applications, 107 (2022), pp. 29–44.
- [79] J. YOU, Y. JIAO, X. LU, AND T. ZENG, *A nonconvex model with minimax concave penalty for image restoration*, Journal of Scientific Computing, 78 (2019), pp. 1063–1086.
- [80] T. ZHANG, J. CHEN, C. WU, Z. HE, T. ZENG, AND Q. JIN, *Edge adaptive hybrid regularization model for image deblurring*, Inverse Problems, 38 (2022), p. 065010.
- [81] D. ZOSSO, J. AN, J. STEVICK, N. TAKAKI, M. WEISS, L. S. SLAUGHTER, H. H. CAO, P. S. WEISS, AND A. L. BERTOZZI, *Image segmentation with dynamic artifacts detection and bias correction*, Inverse Problems and Imaging, 11 (2017), pp. 577–600.